Geophysical Journal International

Geophys. J. Int. (2012) **189,** 1103–1124 doi: 10.1111/j.1365-246X.2012.05416.x

Adjoint analysis of the source and path sensitivities of basin-guided waves

Steven M. Day,[1] Daniel Roten[2] and Kim B. Olsen[1]

[1] *Department of Geological Sciences, San Diego State University, San Diego, CA* 92182*, USA. E-mail: day@moho.sdsu.edu*
[2] *Swiss Seismological Service, ETH Zurich,* CH-8092 *Zurich, Switzerland*

Accepted 2012 February 8. Received 2012 February 7; in original form 2011 July 28

SUMMARY

Simulations of earthquake rupture on the southern San Andreas Fault (SAF) reveal large amplifications in the San Gabriel and Los Angeles Basins (SGB and LAB) apparently associated with long-range path effects. Geometrically similar excitation patterns can be recognized repeatedly in different SAF simulations (e.g. Love wave-like energy with predominant period around 4 s, channelled southwestwardly from the SGB into LAB), yet the amplitudes with which these distinctive wavefield patterns are excited change, depending upon source details (slip distribution, direction and velocity of rupture). We describe a method for rapid calculation of the sensitivity of such predicted wavefield features to perturbations of the source kinematics, using a time-reversed (adjoint) wavefield simulation. The calculations are analogous to those done in adjoint tomography, and the same time-reversed calculation also yields path-sensitivity kernels that give further insight into the excitation mechanism. For rupture on the southernmost 300 km of SAF, LAB excitation is greatest for slip concentrated between the northern Coachella Valley and the transverse ranges, propagating to the NE and with rupture velocities between 3250 and 3500 m s^{-1} along that fault segment; that is, within or slightly above the velocity range (between Rayleigh and *S* velocities) that is energetically precluded in the limit of a sharp rupture front, highlighting the potential value of imposing physical constraints (such as from spontaneous rupture models) on source parametrizations. LAB excitation is weak for rupture to the SW and for ruptures in either direction located north of the transverse transverse ranges, whereas Ventura Basin (VTB) is preferentially excited by NE ruptures situated north of the transverse ranges. Path kernels show that LAB excitation is mediated by surface waves deflected by the velocity contrast along the southern margin of the transverse ranges, having most of their energy in basement rock until they impinge on the eastern edge of SGB, through which they are then funnelled into LAB. VTB amplification is enhanced by a similar waveguide effect.

Key words: Numerical solutions; Earthquake ground motions; Guided waves; Computational seismology; Wave propagation.

1 INTRODUCTION

Numerical simulations of earthquake ground motion have begun to play a significant role in the practical assessment and analysis of earthquake hazard and risk. Ground motion simulations have potential roles in earthquake preparedness planning, engineering studies and probabilistic seismic hazard analysis (PSHA). For example, a recent emergency response and preparedness exercise, the 2008 ShakeOut project (Jones *et al.* 2008), examined the implications of a major (*M*7.8) San Andreas Fault (SAF) earthquake in southern California on the basis of simulated ground motion estimates (Graves *et al.* 2008). This and similar scenario simulations have also provided a basis for engineering estimates of physical damage to structures (e.g. Krishnan *et al.* 2006a,b; Muto & Krishnan 2011), and large ensembles of such simulations are being explored as a supplement to empirical ground motion estimation, with potential applications in PSHA (Graves *et al.* 2010). Numerical simulations are, of course, likely to be of greatest utility for the analysis of scenarios that are poorly represented by existing strong motion records. This criterion suggests a focus on very large, rare events, which therefore implies calculations undertaken at very large spatial scales. Likewise, simulations have particular relevance when regional geology is strongly heterogeneous, and especially when deep and/or laterally extensive sedimentary basins are present (e.g. Frankel & Vidale 1992; Olsen *et al.* 1995; Graves *et al.* 1998; Pitarka *et al.* 1998; Olsen 2000; Komatitsch *et al.* 2004; Day *et al.* 2008a).

Moreover, recent studies have in some cases predicted unexpectedly large, localized amplifications when both of the foregoing factors are present, that is, when very large ruptures interact over large spatial scales with extensive, low-velocity sedimentary structures. For example, calculations by Olsen *et al.* (2006) for a *M*7.7 rupture scenario on the southern SAF suggest that surface wave energy can be redirected into the urban Los Angeles Basin by sedimentary structures present along the southern margin of the transverse ranges (e.g. Magistrale *et al.* 2000; Suss & Shaw 2003), exhibiting some wavefield features reminiscent of a heterogeneous waveguide. However, the same study, in combination with subsequent ones (Graves *et al.* 2008; Olsen *et al.* 2008, 2009; Ely *et al.* 2010), shows that predicted ground motion levels in these highly amplified zones can be very sensitive to some of the specific characteristics of the hypothesized SAF earthquake, as we discuss further in the next section.

These results underscore the need for parameter studies that explore the sensitivity of ground motion phenomenology to source and path variations. We will follow convention (e.g. Weldon *et al.* 2005; Graves *et al.* 2008; Jones *et al.* 2008) in using the term 'scenario' to refer to a hypothesized earthquake whose specification includes the fault, the endpoints of the rupture and the amount and timing of slip as a function of position (or an implied specification of the latter in terms of stresses and frictional parameters in a fully dynamic rupture model, as in, e.g. Olsen *et al.* 2008, 2009; Ely *et al.* 2010). Practical engineering application of simulated ground motion usually requires some characterization of the scenario as a member of a hypothetical ensemble of plausible events (e.g. all scenarios with a given magnitude and rupture endpoints on a given fault). For example, in some applications it may be appropriate to use motion that is representative of a near-worst case scenario (for a given site, fault segment and magnitude), whereas in other applications we may require a scenario that is representative of median-level ground motion for the ensemble. The appropriate ranking of a scenario within such a spectrum of plausible cases may be far from obvious when the source is large and complex and the wave paths traverse complex 3-D Earth structure.

For the class of problems emphasized in the foregoing discussion, the large geographical scale relative to wavelengths of interest, and therefore large computational scale (and cost) required for ground motion simulations, may inhibit parameter studies that are extensive enough to adequately explore parameter sensitivities. And, at best, only limited guidance for navigating through parameter space will be available from conventional wave propagation theory, because it is in just such problems that our customary conceptual tools such as normal mode and ray decompositions lose much of their utility. There is a need to augment those conceptual tools with additional approaches for extracting more general insights from ground motion simulations.

This paper highlights one approach that we have found useful. It is based upon identifying and isolating a wavefield feature of interest within a simulation—here we have in mind wavefield components, such as sedimentary basin excitations, that possesses some recognizably coherent space–time structure—and then calculating both the source- and path-parameter sensitivities (to first order in their respective perturbations) of some scalar measure of the feature. The latter step is executed via time-reversal imaging, that is, an adjoint operation that takes as its source a portion of the simulated wavefield. Section 2 provides additional motivation by reviewing some issues raised by recent simulations for southern California. The theory, with results formally paralleling those underlying adjoint tomography, is outlined in Sections 3–5 and three appendices. Section 6 presents applications of this scheme to a simulation of a large SAF earthquake, including a comparison of the adjoint results with partial forward simulations. Section 7 summarizes results and notes possible extensions and limitations of the adjoint analysis.

2 BACKGROUND

The SAF in southern California has not ruptured in a major earthquake since the 1857 Fort Tejon earthquake, and its southernmost (Coachella) section has not experienced a large event in roughly 300 years (Sieh & Williams 1990). Thus, there are no instrumental records to provide ground motion estimates for a future southern SAF earthquake. Meanwhile, the Working Group on California Earthquake Probabilities (2008) estimates a relatively high 30-yr probability of 37 per cent for such an event (of *M*7.5 or greater). In the absence of recorded ground motion for large SAF events, numerical ground motion simulations (e.g. Olsen *et al.* 1995, 2006, 2008, 2009; Graves *et al.* 1998, 2008; Krishnan *et al.* 2006a,b; Cui *et al.* 2010; Ely *et al.* 2010) have provided some important insights, while also raising new questions.

The most startling predictions originate from simulations of large (*M*7.7 and larger) NW-directed ruptures on the southernmost 200 km of the SAF, for which the calculations of Olsen *et al.* (2006, 2008) show anomalously high long-period (4–5 s) ground motion in parts of the San Gabriel and Los Angeles Basins (SGB and LAB; Fig. 1). Subsequent simulations for similar SAF scenarios have confirmed those predictions (Graves *et al.* 2008; Olsen *et al.* 2009; Ely *et al.* 2010). Several observations are relevant here. (i) Predicted peak ground velocity (PGV) levels for this high-amplitude zone, more than 50 km from the SAF, are in some cases comparable to those immediately adjacent to the fault and can exceed median empirical predictions by 2, and locally up to 3, standard deviations of the natural logarithm (those figures are for the scenario of Olsen *et al.* 2008; other source models lead to even more extreme predictions, e.g. Olsen *et al.* 2006; Graves *et al.* 2008). (ii) Moreover, those levels of exceedance are calculated after the empirical predictions (Campbell & Bozorgnia 2008) have already been corrected upward for the mean basin amplification effect derived from a large suite of simulations for other fault-rupture scenarios in southern California (Day *et al.* 2008a). Thus, the high levels are not easily understood as a purely local amplification effect, but rather appear to require an explanation that considers the entire seismic wave path specific to the southern SAF events. (iii) The high amplitudes are not a result of anomalously high source excitation, because simulated PGV values on rock sites closely track median empirical predictions (see Olsen *et al.* 2008, fig. 15; also Olsen *et al.* 2009). (iv) The high amplitudes are clearly related to rupture–propagation-induced directivity, because the effect is far larger for NW-directed than for SE-directed SAF rupture. However the relationship is not the conventional one, because, as Fig. 1 makes clear, the region of high amplitudes is well to the west of the expected forward directivity cone for SAF ruptures.

The explanation proposed by Olsen *et al.* (2006) is that the high amplitude zone results from a waveguide-like effect, in which the NW-directed forward directivity pulse from a SAF rupture is diverted westward by the sequence of contiguous sedimentary basins lying along the southern edge of the transverse ranges (fig. 2 of Olsen *et al.* 2006). In this conceptual picture, the high amplitudes result from the addition of these channelled waves to basin waves derived locally through other wave interactions at the SGB/LAB edges. This picture emerges quite suggestively in time-sequential

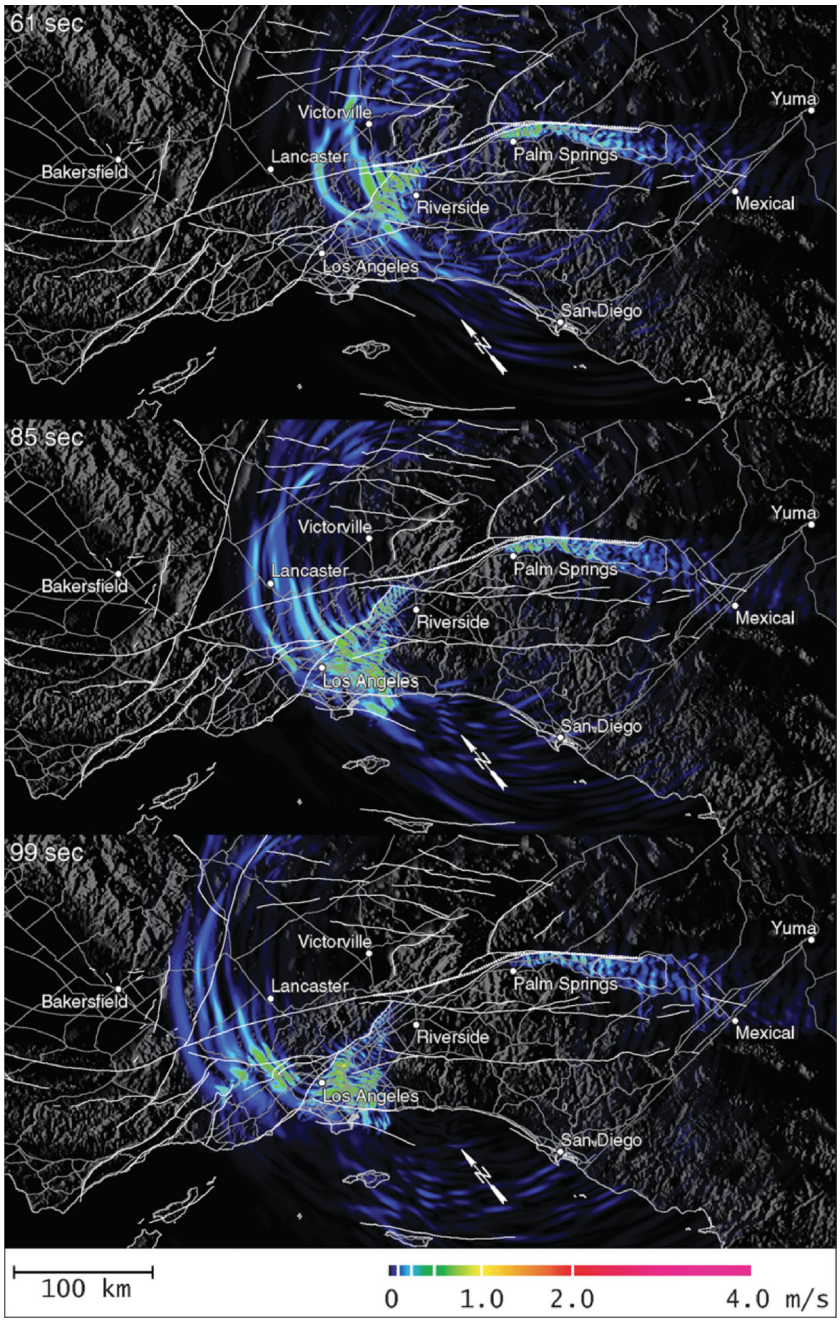

Figure 1. Snapshots of ground-velocity amplitude for simulation of rupture of the southernmost 200 km of the SAF (from Olsen *et al.* 2008). White lines show fault traces and county lines. The dotted line shows the part of the SAF that ruptured (from SE to NW) in the simulation. The very high amplitudes in the SGB and LAB become greatly reduced when rupture directivity is reversed. Although SGB/LAB amplitudes are controlled by rupture directivity, they lie outside the directivity cone predicted for a laterally uniform Earth structure.

wavefield visualizations, as in Fig. 1. However, it remains a qualitative interpretation (which we revisit in Section 6), and it initially proved difficult to project how the anomalous basin-excitation levels would respond to source variations, except through the brute force expedient of repeatedly recalculating full-scale simulations. For example, Olsen *et al.* (2008) used a dynamic rupture model to calculate ground motion from a M7.7 SAF event, and compared calculated amplitude levels in the high-amplitude zone with calculated levels for a kinematic source with slip distribution identical to that of the dynamic model, but constrained to have constant rupture velocity; they found the latter to predict PGV almost a factor of two higher than the former. Olsen *et al.* (2009), comparing their predictions for the M7.8 ShakeOut scenario (Jones *et al.* 2008) with those of Graves *et al.* (2008), found a similar discrepancy, the Olsen *et al.* dynamic rupture sources yielding 3 s spectral accelerations roughly a factor of two lower in the high-amplitude zone than the Graves *et al.* kinematic sources. This was the case even though statically (i.e. in terms of their smoothed, along-strike moment distributions), the sources would have been barely distinguishable. Graves *et al.* note that the SGB/LAB region amplitudes are very sensitive to

rupture velocity, again suggesting that the high amplitudes are directivity related, despite their location far from the SAF and well outside the conventional directivity cone.

In short, the mechanisms for these complex variations in excitation of the SGB/LAB region are not transparent and conventional approximate methods give us minimal help in estimating parametric uncertainties. Very large simulation suites could overcome this difficulty, but this approach remains an impractical one in problems of very large computational scale. Our purpose is to present a methodology that can efficiently provide first-order estimates of source- and path-parameter sensitivities of significant ground motion amplification features, as well as qualitative insights into the source–path interactions that control those sensitivities. Those estimates and insights may then become a guide to more selective parametric studies.

3 GENERAL FRAMEWORK

We treat ground motions in the context of linear dynamic viscoelasticity, with sources given by kinematically prescribed velocity discontinuities on a fault surface. We refer to the simulation under study as the reference simulation, and quantify the degree of excitation of a feature of interest within the reference wavefield by defining a functional E on the velocity field (with space–time support localized to the feature of interest). Then a second (adjoint) simulation, with a source derived from the time reversal of the reference simulation, permits us to calculate perturbations to that functional arising from perturbations to the source.

There is a close analogy with adjoint tomography (e.g. Tarantola 1988; Akcelik 2003; Tromp *et al.* 2005) in our approach. The equivalent-force system of the propagating velocity discontinuity is analogous to the tomographic source; the functional E is analogous to the data misfit function of adjoint tomography, with its Fréchet derivative providing the source term for the adjoint field. As this analogy suggests, the same time-reversed simulation that gives the source sensitivities of E also yields the sensitivity of E to elastic moduli perturbations, providing an image of the principal propagation pathways and modes by which the feature is excited.

3.1 Function spaces

We let Ω denote a bounded, open domain in $\mathbb{R}^3$, $\partial\Omega$ its boundary (assumed smooth, with outward normal $\hat{\mathbf{n}}$) and Σ a surface (smooth, with positive-side normal $\hat{\boldsymbol{\upsilon}}$) contained in $\bar{\Omega}$ and across which jump discontinuities are permitted. We will make reference to the following space–time regions and boundary sets (in which tildas are used to indicate exclusion of the discontinuity surface Σ and overbars indicate closure of a set)

$$\tilde{\Omega} \equiv \bar{\Omega} - \Sigma, \tag{1a}$$

$$\partial\tilde{\Omega} \equiv \partial\Omega - \partial\Omega \cap \Sigma, \tag{1b}$$

$$R \equiv \tilde{\Omega} \times [0, T], \tag{1c}$$

$$\Gamma_1 \equiv \partial\tilde{\Omega} \times [0, T], \tag{1d}$$

$$\Gamma_2 \equiv \Sigma \times [0, T], \tag{1e}$$

$$\Gamma_3 \equiv \tilde{\Omega}, \tag{1f}$$

(the last of which, although redundant, allows us to use a consistent indexing in referring to the various space–time sets that bound R and the corresponding function spaces).

In order for functionals on the velocity field to make sense, we have to restrict consideration to velocity fields that have a certain degree of regularity. We assume that the space of admissible sources (slip functions) has been restricted *a priori* such that all admissible sources generate velocity fields in some space V of vector-valued functions on R (noting that R excludes interior surface Γ_2). We take V such that $\mathbf{w} \in V$ and its first- and second-order partial derivatives are continuous and square-integrable on R. On Γ_2, $\mathbf{w}(\mathbf{x}, t)$ and its normal derivative must have finite positive- and negative-side limits, but opposing-side limits may differ, permitting discontinuity across that boundary. Restrictions of $\mathbf{w}$ and its first-order partial derivatives to $\Gamma_1, \Gamma_3 \times \{0\}$ and $\Gamma_3 \times \{T\}$ are well defined by continuity. V^* denotes the space of linear functionals on V and functionals in V^* will be distinguished by asterisk superscripts.

Elements of V are also in the space H of square-integrable vector-valued functions on R, as are their first and second time derivatives. We give H the inner product

$$(\mathbf{f}, \mathbf{g})_H \equiv \int_{\tilde{\Omega}} \mathrm{d}V \int_0^T \mathbf{f} \cdot \mathbf{g} \mathrm{d}t, \quad \mathbf{f}, \mathbf{g} \in H, \tag{2}$$

where the integrand is the ordinary vector dot product, given in Cartesian coordinates by $\sum_{i=1}^{3} \mathbf{f}_i \mathbf{g}_i$ (we also assume that V has a norm and that the norm in H is bounded by that in V, so the identity mapping from V to H is bounded, a result required in Appendix B). We also use an abbreviated notation for the space–time integral of the scalar product of second-order tensor-valued functions $\boldsymbol{p}$ and $\boldsymbol{q}$ (with square-integrable components),

$$[\boldsymbol{p}, \boldsymbol{q}]_{H\otimes H} \equiv \int_{\tilde{\Omega}} \mathrm{d}V \int_0^T \boldsymbol{p} : \boldsymbol{q} \mathrm{d}t, \tag{3}$$

(where the integrand is the ordinary tensor scalar product, given in Cartesian coordinates by $\sum_{i=1}^{3} \sum_{j=1}^{3} \boldsymbol{p}_{ij} \boldsymbol{q}_{ij}$). We denote by B_1, B_2 and B_3 the square-integrable functions on Γ_1, Γ_2 and Γ_3, respectively, with the following inner products over these boundary domains,

$$(\mathbf{f}, \mathbf{g})_{B_1} \equiv \int_{\partial\tilde{\Omega}} \mathrm{d}A \int_0^T \mathbf{f} \cdot \mathbf{g} \mathrm{d}t, \quad \mathbf{f}, \mathbf{g} \in B_1, \tag{4a}$$

$$(\mathbf{f}, \mathbf{g})_{B_2} \equiv \int_{\Sigma} \mathrm{d}A \int_0^T \mathbf{f} \cdot \mathbf{g} \mathrm{d}t, \quad \mathbf{f}, \mathbf{g} \in B_2, \tag{4b}$$

$$(\mathbf{f}, \mathbf{g})_{B_3} \equiv \int_{\tilde{\Omega}} \mathrm{d}V \, \mathbf{f} \cdot \mathbf{g}, \quad \mathbf{f}, \mathbf{g} \in B_3. \tag{4c}$$

A convolution operator $*$ between vectors will imply temporal convolution combined with contraction, with the component products in the contraction operation interpreted as convolutions of the respective components, for example $\mathbf{f} * \mathbf{g}$ is defined by

$$\mathbf{f} * \mathbf{g}\ (\mathbf{x}, t) \equiv \int_0^t \mathbf{f}(\mathbf{x}, \tau) \cdot \mathbf{g}(\mathbf{x}, t - \tau) \mathrm{d}\tau. \tag{5a}$$

When there is a double contraction as well as convolution, we will show that explicitly, for example $\boldsymbol{p} : *\boldsymbol{q}$ means

$$\boldsymbol{p} : *\boldsymbol{q}\ (\mathbf{x}, t) \equiv \int_0^t \boldsymbol{p}(\mathbf{x}, \tau) : \boldsymbol{q}(\mathbf{x}, t-\tau)\, \mathrm{d}\tau. \tag{5b}$$

The notations $\tilde{\Omega}^T$ and Σ^T will be used to indicate volume and surface integrals for which the integrand has been evaluated at $t = T$, for example

$$\int_{\tilde{\Omega}^T} \mathrm{d}V\, \mathbf{f} * \mathbf{g} \equiv \int_{\tilde{\Omega}} \mathrm{d}V\ (\mathbf{f} * \mathbf{g})|_{t=T} = (\mathbf{f}, \Pi\mathbf{g})_H\,, \quad \mathbf{f}, \mathbf{g} \in H, \tag{6a}$$

$$\int_{\Sigma^T} \mathrm{d}A\, \mathbf{f} * \mathbf{g} \equiv \int_{\Sigma} \mathrm{d}A\ (\mathbf{f} * \mathbf{g})|_{t=T} = (\mathbf{f}, \Pi\mathbf{g})_{B_2}, \quad \mathbf{f}, \mathbf{g} \in B_2, \tag{6b}$$

(and similarly for integration on Γ_1, or for integration of doubly contracted products such as eq. 5b), where Π symbolizes time reversal,

$$\Pi\mathbf{f}(\mathbf{x}, t) = \mathbf{f}(\mathbf{x}, T-t). \tag{7}$$

3.2 Anelasticity

In linear viscoelasticity, the stress tensor $\boldsymbol{T}$ is a hereditary integral over strain-rate history $\dot{\boldsymbol{e}}$, of the form

$$\boldsymbol{T}(\mathbf{x}, t) = \int_{-\infty}^t \boldsymbol{c}(\mathbf{x}, t-\tau) : \dot{\boldsymbol{e}}(\mathbf{x}, \tau)\, \mathrm{d}\tau, \tag{8}$$

where the time-dependent fourth-order tensor $\boldsymbol{c}$ consists of a time-independent unrelaxed modulus, $\boldsymbol{c}_u(\mathbf{x})$, minus a time-dependent relaxation function $\boldsymbol{c}_u(\mathbf{x}) - \boldsymbol{c}(\mathbf{x}, t)$ that has initial value zero. We assume that $\boldsymbol{c}$ has the symmetries $\boldsymbol{c}_{ijpq} = \boldsymbol{c}_{jipq} = \boldsymbol{c}_{pqij}$, implying also $\boldsymbol{c}_{ijpq} = \boldsymbol{c}_{ijqp}$. Using definition (5b), (8) can be written, for $t \geq 0$, as

$$\boldsymbol{T}(\mathbf{x}, t) = \int_{-\infty}^0 \boldsymbol{c}(\mathbf{x}, t-\tau) : \dot{\boldsymbol{e}}(\mathbf{x}, \tau)\, \mathrm{d}\tau + \boldsymbol{c}(\mathbf{x}, t) : *\dot{\boldsymbol{e}}(\mathbf{x}, t). \tag{9}$$

The first term is a stress history representing relaxation of stresses associated with the strain history on time interval $(-\infty, \mathbf{0})$. We denote that initial strain history by $\boldsymbol{e}^<$ and redefine $\boldsymbol{e}$ and $\boldsymbol{T}$ to be restrictions of the strain and stress histories, respectively, to the time interval $[0, T]$. We can then write the stress as

$$\boldsymbol{T}(\mathbf{x}, t) = \boldsymbol{T}^>(\mathbf{x}, t) + \boldsymbol{c}(\mathbf{x}, t) : *\dot{\boldsymbol{e}}(\mathbf{x}, t),\ t \in [0, T], \tag{10}$$

where

$$\boldsymbol{T}^>(\mathbf{x}, t) = \int_{-\infty}^0 \boldsymbol{c}(\mathbf{x}, t-\tau) : \dot{\boldsymbol{e}}^<(\mathbf{x}, \tau)\, d\tau,\ t \in [0, T], \tag{11}$$

(note that $\boldsymbol{T}^>$ is a function of non-negative time, representing the relaxation of stresses induced by strain $\boldsymbol{e}^<$ already accrued during negative time). The assumed symmetries of $\boldsymbol{c}$ permit us to replace the strain rate with the gradient of velocity $\mathbf{v}$, and it is also convenient to work with stress rate, expressing it in terms of a distributional time derivative of $\boldsymbol{c}$, so we write the time derivative of (10) as

$$\dot{\boldsymbol{T}} = \dot{\boldsymbol{T}}^> + \dot{\boldsymbol{C}} : *\nabla\mathbf{v}, \tag{12}$$

where now all quantities are defined on the time interval $[0, T]$ and we have introduced the notation

$$\dot{\boldsymbol{C}}(\mathbf{x}, t) \equiv c_u(\mathbf{x})\, \delta(t) + \dot{c}(\mathbf{x}, t) \tag{13}$$

(and the lower limit of the convolution integral is understood to be 0^-). Tensor $\boldsymbol{C}$ is the same as $\boldsymbol{c}$ except that the former is understood to account for the initial value contribution in a way that permits time differentiation to be shifted from the strain rate to the modulus tensor, which is simply a notational device to render the equations of motion in a form similar to that of the elastodynamic case (and later to make an operator symmetry more transparent).

In general, to fully specify the initial state determining motion on time interval $[0, T]$, it is necessary to give the function $\boldsymbol{e}^<$, or $\boldsymbol{T}^>$. However, we restrict consideration to so-called anelastic models (in the sense of, e.g. Nowick & Berry 1972), by requiring that, after a sufficiently long time $\boldsymbol{t}_R$, $\boldsymbol{c}$ differ negligibly from some equilibrium value, the relaxed modulus $\boldsymbol{c}_R(\mathbf{x})$, so that an equilibrium stress state exists for any strain state. If the strain rate is negligible during time interval $(-\boldsymbol{t}_R, 0)$, then equilibrium will have been reached at $t = 0$, with $\boldsymbol{T}^>$ simply reducing to a time-independent initial stress field, that is

$$\boldsymbol{T}^>(\mathbf{x}, t) = \int_{-\infty}^0 \boldsymbol{c}(\mathbf{x}, t-\tau) : \dot{\boldsymbol{e}}^<(\mathbf{x}, \tau)\, \mathrm{d}\tau \approx \boldsymbol{c}_R(\mathbf{x}) : \times \int_{-\infty}^0 \dot{\boldsymbol{e}}^<(\mathbf{x}, \tau)\, \mathrm{d}\tau = \boldsymbol{T}(\mathbf{x}, 0), \tag{14}$$

and in that case $\dot{\boldsymbol{T}}^> = 0$ and (12) reduces to $\dot{\boldsymbol{T}} = \dot{\boldsymbol{C}} : *\nabla\mathbf{v}$. We will assume that the reference simulation is initiated in such a fully relaxed state, with $\dot{\boldsymbol{T}}^> = 0$.

We, in addition, require components of $\boldsymbol{c}$ to be twice continuously differentiable in time and continuously differentiable in the space coordinates, apart from a possible jump discontinuity on Γ_2, where positive- and negative-side limits are denoted by superscripts, for example $\dot{\boldsymbol{C}}^{\pm}$. We further restrict the relaxation function to be such that positive work is done in any deformation path starting from an unstrained state, and require components of $\boldsymbol{c}_u$ to be non-zero. These conditions are sufficient (Gurtin & Sternberg 1963) to meet the requirement in Appendix A that (12) be invertible to give the strain rate in terms of stress rate,

$$\dot{\boldsymbol{e}} = \dot{\boldsymbol{e}}^> + \dot{\boldsymbol{J}} : *\dot{\boldsymbol{T}} \tag{15}$$

($\dot{\boldsymbol{e}}^>$ is the creep rate on $[0, T]$ due to stress accrued during $(-\infty, 0)$ and $\dot{\boldsymbol{J}}$ has the same relation to the creep function that $\dot{\boldsymbol{C}}$ has to $\boldsymbol{c}$ in eq. 13).

3.3 Boundary functions

To keep track of the functions created by various boundary-set restrictions of functions $\mathbf{w} \in V$, we symbolize those restrictions by trace operators $\gamma_j : V \to B_j$, with added superscripts distinguishing different operators associated with a common boundary. These are

$$\gamma_1\mathbf{w} = \mathbf{w}|_{\Gamma_1} \in B_1, \text{ the restriction of } \mathbf{w} \text{ to } \Gamma_1; \tag{16}$$

$$\gamma_2\mathbf{w} = \left(\gamma_2^+\mathbf{w}, \gamma_2^-\mathbf{w}\right) \in B_2 \times B_2, \tag{17a}$$

where $\gamma_2^+\mathbf{w}$ and $\gamma_2^-\mathbf{w}$ are the positive- and negative-sides limits at Γ_2, respectively, from which we also define

$$\gamma_2^\Delta\mathbf{w} = \gamma_2^+\mathbf{w} - \gamma_2^-\mathbf{w}, \text{ discontinuity on } \Gamma_2, \tag{17b}$$

$$\gamma_2^{\alpha}\mathbf{w} = \alpha\gamma_2^{+}\mathbf{w} + (1-\alpha)\,\gamma_2^{-}\mathbf{w}\,, \text{ weighted mean on } \Gamma_2, \tag{17c}$$

with $\alpha(\mathbf{x})$ denoting any bounded, real scalar-valued function defined on Σ; and

$$\gamma_3\mathbf{w} = \left(\gamma_3^{I}\mathbf{w}, \gamma_3^{F}\mathbf{w}\right) \in B_3 \times B_3, \tag{18a}$$

where

$$\gamma_3^{I}\mathbf{w} = \mathbf{w}|_{\Gamma_3\times\{0\}} \in B_3, \text{ restriction of } \mathbf{w} \text{ to } \Gamma_3 \times \{0\}\,, \text{ that is, its initial-value function; and} \tag{18b}$$

$$\gamma_3^{F}\mathbf{w} = \mathbf{w}|_{\Gamma_3\times\{T\}} \in B_3, \text{ restriction of } \mathbf{w} \text{ to } \Gamma_3 \times \{T\}\,, \text{ that is, its final-value function.} \tag{18c}$$

We introduce three more operators $\beta_j : V \to B_j$ that return functions in B_1, B_2 or B_3. The first two map velocities to boundary traction rates, excluding any contribution from $\boldsymbol{T}^{>}$,

$$\beta_1\mathbf{w} = \hat{\mathbf{n}}\cdot\dot{\boldsymbol{C}} : *(\nabla\mathbf{w})|_{\Gamma_1} \in B_1, \text{ traction rate on } \Gamma_1 \text{ (excluding } \hat{\mathbf{n}}\cdot\dot{\boldsymbol{T}}^{>}\text{)}; \tag{19}$$

and

$$\beta_2\mathbf{w} = \left(\beta_2^{+}\mathbf{w}, \beta_2^{-}\mathbf{w}\right) \in B_2 \times B_2, \tag{20a}$$

where

$$\beta_2^{\pm}\mathbf{w} = \hat{\upsilon}\cdot\left[\dot{\boldsymbol{C}}^{\pm} : *(\nabla\mathbf{w})|_{\Gamma_2^{\pm}}\right], \tag{20b,c}$$

from which we also define

$$\beta_2^{\Delta}\mathbf{w} = \beta_2^{+}\mathbf{w} - \beta_2^{-}\mathbf{w}\,, \text{ traction-rate jump on } \Gamma_2 \text{ (excluding } \hat{\boldsymbol{\upsilon}}.\dot{\boldsymbol{T}}^{>}\text{)}, \tag{20d}$$

$$\beta_2^{\alpha}\mathbf{w} = \alpha\beta_2^{+}\mathbf{w} + (1-\alpha)\,\beta_2^{-}\mathbf{w}, \text{ weighted mean traction rate on } \Gamma_2 \text{ (excluding } \hat{\boldsymbol{\upsilon}}.\dot{\boldsymbol{T}}^{>}\text{)}. \tag{20e}$$

The third gives endpoint time derivatives weighted by density,

$$\beta_3\mathbf{w} = \left(\beta_3^{I}\mathbf{w}, \beta_3^{F}\mathbf{w}\right) \in B_3 \times B_3, \tag{21a}$$

where

$$\beta_3^{I}\mathbf{w} = \rho\,\partial_t\mathbf{w}|_{\Gamma_3\times\{0\}}\,, \text{ density times initial acceleration,} \tag{21b}$$

$$\beta_3^{F}\mathbf{w} = \rho\,\partial_t\mathbf{w}|_{\Gamma_3\times\{T\}}\,, \text{ density times final acceleration.} \tag{21c}$$

(and density ρ is a continuous, positive function of the spatial coordinates). The definitions of the weighted-mean operators γ_2^{α} and β_2^{α} are motivated by their utility for restating expressions such as $\gamma_2^{+}\mathbf{u}\cdot\beta_2^{+}\mathbf{w} - \gamma_2^{-}\mathbf{u}\cdot\beta_2^{-}\mathbf{w}$ in terms of the discontinuities $\gamma_2^{\Delta}\mathbf{u}$ and $\beta_2^{\Delta}\mathbf{w}$,

$$\gamma_2^{+}\mathbf{u}\cdot\beta_2^{+}\mathbf{w} - \gamma_2^{-}\mathbf{u}\cdot\beta_2^{-}\mathbf{w} = \gamma_2^{\alpha}\mathbf{u}\cdot\beta_2^{\Delta}\mathbf{w} + \gamma_2^{\Delta}\mathbf{u}\cdot\beta_2^{1-\alpha}\mathbf{w}. \tag{22}$$

4 INITIAL VALUE PROBLEM OPERATOR AND ITS TRANSPOSE

The relationship between the direct and adjoint problems in dynamic viscoelasticity is well known, but we revisit the question to put it in the present context of evaluating Fréchet derivatives of functionals of the velocity field. Although the final results can be obtained without difficulty using more familiar formalism, there are conceptual advantages in following an approach initiated for elastodynamics by Gurtin (1964), and subsequently simplified by Herrera & Bielak (1974), wherein we express the viscoelastic initial boundary value problem in abstract form as a functional-valued operator equation. In Appendix A, we extend Herrera and Bielak's approach to accommodate viscoelastic response (using Leitman 1966; Herrera & Bielak 1977) and the fault-plane discontinuity. We show, by construction, how the operator achieves symmetry with its transpose while capturing the initial and boundary conditions.

Conceptual advantages, include the following: (i) the operator is expressed in terms of a single bilinear functional that accounts for all discontinuity jumps, boundary conditions and initial conditions, without requiring any of these to be carried as *a priori* constraints on the operator domain, thus making the self-transpose character of the initial-value problem transparent. (ii) We do not explicitly introduce a generalized function for moment density (which requires a smooth viscoelastic modulus function at sites where the moment density is singular, as noted by Backus & Mulcahy 1976), so the formulation remains valid even when part of the fault coincides with a surface of discontinuity of the elastic modulus. The source functional arises naturally from the kinematic boundary condition (and the nature of the ambiguity in the moment–tensor formalism noted by others, e.g. Heaton & Heaton 1989, Ampuero & Dahlen 2005, becomes immediately apparent). (iii) The other sources of interest to us fit this conceptual framework quite naturally as well; for example, we will quantify wavefield features by means of functionals and these, through their Fréchet derivatives, serve, in this formalism, as sources for the adjoint field.

4.1 Initial, boundary and discontinuity conditions

We will consider reference simulations for which the velocity field $\mathbf{v} \in V$ (i) satisfies the homogeneous integro-differential equations of linear dynamic viscoelasticity on space–time region R; (ii) has jump discontinuity and continuous traction, on Γ_2; (iii) has zero traction on external boundary Γ_1 and (iv) is initially in static equilibrium (i.e. has zero velocity and acceleration on $\Gamma_3 \times \{t = 0\}$, implying that stresses due to pre-existing strains have fully relaxed, so $\boldsymbol{T}^{>}$ is just a constant $\boldsymbol{T}_0 = \boldsymbol{c}_R : \boldsymbol{e}^{<}|_{t=0}$, with $-\nabla\cdot\boldsymbol{T}_0$ equal to the product of density and the gravitational acceleration).

We begin with a somewhat more general viscoelastic problem, and write the equations of motion in time-differentiated form (for convenience, because various static quantities like gravitational acceleration and fiducial stresses and displacements can then be ignored). We refer to functions $(\mathbf{v}_{\text{init}}, \mathbf{a}_{\text{init}}, \mathbf{e}^{<})$ as initial-state conditions. Here $\mathbf{v}_{\text{init}}$ and $\mathbf{a}_{\text{init}}$ are specified initial velocity and acceleration, respectively, on $\Gamma_3 \times \{0\}$, and (as before) $\boldsymbol{e}^{<}$ is strain history on $\Gamma_3 \times (-\infty, 0)$. The latter is associated, through (11), with stress $\boldsymbol{T}^{>}$ (on R); $\mathbf{T}_n^{>}$ will denote $\hat{\mathbf{n}}\cdot\boldsymbol{T}^{>}$(on Γ_1) and $\Delta\mathbf{T}_{\upsilon}^{>}$ will denote $\hat{\boldsymbol{\upsilon}}\cdot(\boldsymbol{T}^{>+} - \boldsymbol{T}^{>-})$ (on Γ_2). The functions $(\mathbf{v}_{\text{init}}, \mathbf{a}_{\text{init}}, \boldsymbol{T}^{>})$ are an equivalent specification of the initial-state conditions.

We permit a body force-rate density $-\nabla\cdot\boldsymbol{p} + \mathbf{b}$ in R (with $\mathbf{b}(\mathbf{x}, t)$ vector valued and $\boldsymbol{p}(\mathbf{x}, t)$ second-order tensor valued), from which are derived (possibly) non-zero surface traction rate $\mathbf{p}_n \equiv \hat{\mathbf{n}}\cdot\boldsymbol{p}$ on Γ_1 and traction-rate discontinuity $\Delta\mathbf{p}_{\upsilon} \equiv -\hat{\boldsymbol{\upsilon}}\cdot(\boldsymbol{p}^{+} - \boldsymbol{p}^{-})$ on Γ_2. As noted, we also permit a velocity discontinuity $\dot{\mathbf{s}}$ to be specified on Γ_2. Then our problem statement is that $\mathbf{v} \in V$ satisfy

$$\mathcal{L}\mathbf{v} = -\nabla\cdot\boldsymbol{p} + \mathbf{b} + \nabla\cdot\dot{\boldsymbol{T}}^{>}, \quad \nabla\cdot\boldsymbol{p}, \mathbf{b}, \nabla\cdot\dot{\boldsymbol{T}}^{>} \in H \cap Rg\,(\mathcal{L})\,, \tag{23a}$$

$$\beta_1\mathbf{v} = \mathbf{p}_n - \dot{\mathbf{T}}_n^{>}, \quad \mathbf{p}_n, \dot{\mathbf{T}}_n^{>} \in B_1 \cap Rg\,(\beta_1)\,, \tag{23b}$$

$$\gamma_2^{\Delta}\mathbf{v} = \dot{\mathbf{s}}, \quad \dot{\mathbf{s}} \in B_2 \cap Rg\left(\gamma_2^{\Delta}\right), \tag{23c}$$

$$\beta_2^{\Delta}\mathbf{v} = \Delta\mathbf{p}_{\upsilon} - \Delta\dot{\boldsymbol{T}}_{\upsilon}^{>}, \quad \Delta\mathbf{p}_{\upsilon}, \Delta\dot{\boldsymbol{T}}_{\upsilon}^{>} \in B_2 \cap Rg\left(\beta_2^{\Delta}\right), \tag{23d}$$

$$\gamma_3^{I}\mathbf{v} = \mathbf{v}_{\text{init}}, \quad \mathbf{v}_{\text{init}} \in B_3 \cap Rg\left(\gamma_3^{I}\right), \tag{23e}$$

$$\beta_3^{I}\mathbf{v} = \rho\mathbf{a}_{\text{init}}, \quad \mathbf{a}_{\text{init}} \in B_3 \cap Rg\left(\beta_3^{I}\right), \tag{23f}$$

where $\mathcal{L} : V \to H$ is

$$\mathcal{L}\mathbf{v} = \rho\ddot{\mathbf{v}} - \nabla\cdot\left(\dot{\boldsymbol{C}} : *\nabla\mathbf{v}\right) \tag{24}$$

[in addition, it will be implicit that we further restrict the right-hand side functions in (23) such that a solution with the required regularity actually exists].

4.2 Operator form of initial value problem

We next construct from (23) a linear functional (dependent upon $\mathbf{v} \in V$) with the following properties: (i) the functional is zero (i.e. evaluates to zero for all $\mathbf{w} \in V$) if $\mathbf{v} \in V$ satisfies (23); (ii) if, for some $\mathbf{v} \in V$ the functional is zero, then $\mathbf{v}$ satisfies (23) and (iii) the functional has the form $a(\mathbf{v}, \cdot) - f^*$, where $f^* \in V^*$ is a linear functional and $a : V \times V \to \mathbb{R}$ is a bilinear functional that is symmetric in its arguments, that is $a(\mathbf{w}, \mathbf{v}) = a(\mathbf{v}, \mathbf{w})$. Functional f^* is independent of $\mathbf{v}$ and represents a generalized set of sources accounting for the initial-state conditions, as well as imposed body-force densities and boundary conditions (all expressed as rates). We indicate this dependency by writing $f^* = \mathcal{F}[\mathbf{v}_{\text{init}}, \mathbf{a}_{\text{init}}, \boldsymbol{T}^{>}; \boldsymbol{p}, \mathbf{b}, \dot{\mathbf{s}}]$, $\mathcal{F}$ being a mapping from generalized sources to functionals in V^*.

The construction, modelled on Herrera & Bielak (1974), is given in Appendix A (using the notation in eqs 2, 3, 4 and 7 to represent integrations) and the result, (A18) and (A19), is (restated in the notation of eqs 5 and 6)

$$\begin{aligned} a(\mathbf{v}, \mathbf{w}) = &\int_{\tilde{\Omega}^T} \mathrm{d}V \left(\rho\dot{\mathbf{w}} * \dot{\mathbf{v}} + \nabla\mathbf{w} : *\dot{\boldsymbol{C}} : *\nabla\mathbf{v}\right) \\ &+ \int_{\tilde{\Omega}^T} \mathrm{d}V \left(\gamma_3^{I}\mathbf{v}\cdot\beta_3^{F}\mathbf{w} + \gamma_3^{I}\mathbf{w}\cdot\beta_3^{F}\mathbf{v}\right), \\ &+ \int_{\Sigma^T} \mathrm{d}A \left\{\gamma_2^{\Delta}\mathbf{w} * \beta_2^{\alpha}\mathbf{v} + \gamma_2^{\Delta}\mathbf{v} * \beta_2^{\alpha}\mathbf{w}\right\} \end{aligned} \tag{25}$$

and

$$f^*(\mathbf{w}) = \mathcal{F}\left[\mathbf{v}_{\text{init}}, \mathbf{a}_{\text{init}}, \boldsymbol{T}^{>};\ \boldsymbol{p}, \mathbf{b}, \dot{\mathbf{s}}\right](\mathbf{w}), \tag{26}$$

where

$$\begin{aligned} &\mathcal{F}\left[\mathbf{v}_{\text{init}}, \mathbf{a}_{\text{init}}, \boldsymbol{T}^{>};\ \boldsymbol{p}, \mathbf{b}, \dot{\mathbf{s}}\right](\mathbf{w}) \\ &= \int_{\tilde{\Omega}^T} \mathrm{d}V \left(\beta_3^{F}\mathbf{w}\cdot\mathbf{v}_{\text{init}} + \gamma_3^{F}\mathbf{w}\cdot\rho\mathbf{a}_{\text{init}} - \dot{\boldsymbol{T}}^{>} : *\nabla\mathbf{w}\right) \\ &\quad + \int_{\tilde{\Omega}^T} \mathrm{d}V \left[\boldsymbol{p} : *\nabla\mathbf{w} + \mathbf{b} * \mathbf{w}\right] + \int_{\Sigma^T} \mathrm{d}A\,\beta_2^{\alpha}\mathbf{w} * \dot{\mathbf{s}}. \end{aligned} \tag{27}$$

Recall that this notation means that the volume and surface integrals are to be evaluated at time T, and that the operators γ and β indicate the various space–time boundary restrictions defined in (16)–(21). The first integral in (27) represents the equivalent forces of the initial state, the second the applied loads and the third the equivalent forces of the fault slip.

For fixed $\mathbf{v} \in V$ in (25), $a(\mathbf{v}, \cdot)$ is a linear functional, $a(\mathbf{v}, \cdot) \in V^*$, in terms of which we can define a functional-valued linear operator $\mathcal{A} : V \to V^*$, by

$$\mathcal{A}\mathbf{v} = a(\mathbf{v}, \cdot), \quad \forall\mathbf{v} \in V. \tag{28}$$

Then the single equation

$$\mathcal{A}\mathbf{v} = f^*, \quad f^* \in Rg(\mathcal{A}) \subset V^*, \tag{29}$$

between linear functionals $\mathcal{A}\mathbf{v}$ and f^* is equivalent to (23), including all initial-state and boundary conditions. Note that we have assumed that restrictions on the problem inputs have insured that $f^* \in Rg(\mathcal{A})$, and this assumption is implicit in what follows. With the restrictions on C stated in Section 3.2, the solution is unique (e.g. Edelstein & Gurtin 1964) and (29) can be inverted,

$$\mathbf{v} = Gf^*. \tag{30}$$

with inverse $G \equiv \mathcal{A}^{-1}$, $G : V^* \supset Rg(\mathcal{A}) \to V$.

We can also define transposes $\mathcal{A}^t : V \to V^*$ and $G^t : Rg(\mathcal{A}) \to V$, by the relationships

$$\mathcal{A}^t\mathbf{w}(\mathbf{v}) = \mathcal{A}\mathbf{v}(\mathbf{w}), \quad \mathbf{v}, \mathbf{w} \in V, \tag{31}$$

$$g^*(Gf^*) = f^*\left(G^t g^*\right), \quad f^*, g^* \in Rg(\mathcal{A}) \subset V^*, \tag{32}$$

and substitution of $\mathcal{A}\mathbf{v}$ for f^* and $\mathcal{A}^t\mathbf{w}$ for g^* shows that $G^t = (\mathcal{A}^t)^{-1}$. The symmetry $a(\mathbf{v}, \mathbf{w}) = a(\mathbf{w}, \mathbf{v})$ implies

$$\mathcal{A}^t = \mathcal{A},\ G^t = G, \tag{33a,b}$$

a result that is used in Section 5. If we express the dependence on initial-state and source terms as in (26), (33) immediately leads to a concise statement of familiar reciprocity relationships: let ξ_i be the set of initial-state/source terms belonging to solution $\mathbf{v}_i$, $i = 1, 2$; then (25), (26), (29) and (33a) lead to $\mathcal{F}[\xi_1](\mathbf{v}_2) = \mathcal{F}[\xi_2](\mathbf{v}_1)$. An additional consequence of (33), worth noting even though we do not use it, is that this symmetry implies equivalency of (29), and therefore (23), to a variational principle: $\mathbf{v}$ is a solution to (23) if and only if functional $\mathcal{J} \equiv \mathcal{A}\mathbf{w}(\mathbf{w}) - 2f^*(\mathbf{w})$ is stationary at $\mathbf{w} = \mathbf{v}$ (which is essentially just a restatement of a principal result of Herrera & Bielak 1974, 1977, extended to include fault kinematics).

4.3 Source and path perturbations

4.3.1 Source perturbations

We use subscript 0 to indicate functions and operators associated with the reference simulation (but note that subscript 0 is used differently in Appendix A). Thus, the reference velocity field $\mathbf{v}_0$ is solution to (29), with $\mathcal{A} = \mathcal{A}_0$ (and G = G_0), signifying that material properties $\boldsymbol{C}$ and $\boldsymbol{\rho}$ take their respective reference values $\boldsymbol{C}_0$ and $\boldsymbol{\rho}_0$, with source term f_0^* constructed from (26) and (27) with fault slip-rate $\dot{\mathbf{s}}$ equal to $\dot{\mathbf{s}}_0$ and with $\boldsymbol{p}$, $\mathbf{b}$, $\mathbf{v}_{\text{init}}$, $\mathbf{a}_{\text{init}}$ and $\boldsymbol{T}^{>}$ equal to zero. That is,

$$\mathcal{A}_0\mathbf{v}_0 = f_0^*, \tag{34}$$

where

$$f_0^*(\mathbf{w}) = \mathcal{F}\left[0, 0, 0;\ 0, 0, \dot{\mathbf{s}}_0\right](\mathbf{w}) = \int_{\Sigma^T} \mathrm{d}A\,\beta_{20}^{\alpha}\mathbf{w} * \dot{\mathbf{s}}_0, \tag{35}$$

and β_{20}^{α} is β_2^{α} defined by (20e) with reference value of the modulus tensor,

$$\beta_{20}^{\alpha}\mathbf{w} = \hat{\boldsymbol{\upsilon}}\cdot\left[\alpha\left(\dot{\boldsymbol{C}}_0 : *\nabla\mathbf{w}\right)^{+} + (1-\alpha)\left(\dot{\boldsymbol{C}}_0 : *\nabla\mathbf{w}\right)^{-}\right], \tag{36}$$

the superscripts indicating positive- and negative-side values on the fault surface (recall that α is an arbitrary function of position on the fault surface).

If we perturb slip rate by $\delta\dot{\mathbf{s}}$ and call the corresponding velocity-field perturbation $\delta\mathbf{v}_s$, (34) and (35) lead to

$$\mathcal{A}_0\delta\mathbf{v}_s = \delta f_s^*, \tag{37}$$

where

$$\delta f_s^*(\mathbf{w}) = \mathcal{F}[0,0,0;\ 0,0,\delta\dot{\mathbf{s}}](\mathbf{w}) = \int_{\Sigma^T} \mathrm{d}A\ \beta_{20}^{\alpha}\mathbf{w} * \delta\dot{\mathbf{s}}, \tag{38}$$

and the subscript on δf_s^* is a reminder that this source functional arises from a perturbation to slip velocity.

4.3.2 Path perturbations

By path perturbations, we will refer to perturbations to the elastic moduli or wave speeds. Upon substituting perturbation expansions $\boldsymbol{C} = \boldsymbol{C}_0 + \varepsilon\boldsymbol{C}_1 + \cdots$ of the modulus tensor and $\mathbf{v} = \mathbf{v}_0 + \varepsilon\mathbf{v}_1 + \cdots$ of the velocity field into (25) for $a(\mathbf{v},\cdot)$ and into (27) for $\mathcal{F}[0,0,0;\ 0,0;\dot{\mathbf{s}}_0]$, we find that terms first order in ε satisfy an equation of the form $\mathcal{A}_0\mathbf{v}_1 = \eta_1^*$, where $\eta_1^* \in V^*$ depends linearly on $\boldsymbol{C}_1$. Neglecting higher-order terms, we equate $\varepsilon\boldsymbol{C}_1$ to total perturbation $\delta\boldsymbol{C}$ and $\varepsilon\mathbf{v}_1$ to the total velocity perturbation $\delta\mathbf{v}_C$, and obtain the result

$$\mathcal{A}_0\delta\mathbf{v}_C = \delta f_C^*, \tag{39}$$

with path-perturbation functional δf_C^* defined by

$$\delta f_C^*(\mathbf{w}) = \int_{\tilde{\Omega}^T} \mathrm{d}V\left(-\nabla\mathbf{w}\colon * \delta\dot{\mathbf{C}} : *\nabla\mathbf{v_0}\right) - \int_{\Sigma^T} \mathrm{d}A\ \gamma_2^{\Delta}\mathbf{w} * \delta\beta_2^{\alpha}\mathbf{v}_0, \tag{40}$$

where

$$\boldsymbol{\delta}\beta_2^{\alpha}\mathbf{w} = \hat{\boldsymbol{\upsilon}}\cdot\left[\alpha\left(\delta\dot{\boldsymbol{C}} : *\nabla\mathbf{w}\right)^{+} + (1-\alpha)\left(\delta\dot{\boldsymbol{C}} : *\nabla\mathbf{w}\right)^{-}\right]. \tag{41}$$

The subscript on f_C^* indicates that the source functional arises from a perturbation to the modulus tensor.

Eqs (39)–(41) are similar to (37) and (38), with the path-perturbation functional δf_C^* replacing the source-perturbation functional δf_s^* and $\delta\mathbf{v}_C$ replacing $\delta\mathbf{v}_s$. Generalizing, we could perturb with respect to some source or path property χ, tensor-, vector-, or scalar-valued (a scalar-valued example would be the P or S wave speeds, after specializing to an isotropic medium), and end up, to first order, with

$$\mathcal{A}_0\delta\mathbf{v}_\chi = \delta f_\chi^*, \tag{42}$$

for some functional δf_χ^*, (37) and (39) being special cases of (42).

5 WAVEFIELD SENSITIVITIES

Once a wavefield feature of interest (such as one of the prominent basin excitations discussed earlier) has been described in quantitative terms as a functional of the velocity field, its first-order sensitivities to source and path parameters can be expressed in terms of an adjoint field that satisfies (29) (and therefore eqs 23) with an appropriate source term.

5.1 Quantifying wavefield features

We characterize a given wavefield feature through the value $E(\mathbf{v})$ of an excitation functional, $E : V \to \mathbb{R}$, that is non-linear and has as its range the non-negative reals, providing a scalar intensity measure of the wavefield feature. We require E to be Fréchet differentiable at $\mathbf{v}_0$, with Fréchet derivative denoted by $DE(\mathbf{v}_0;\cdot)$, a continuous linear functional, and the first-order variation δE of E in response to velocity perturbation $\mathbf{w}$ is $DE(\mathbf{v}_0;\mathbf{w})$.

For example, to analyse the SGB/LAB excitation mentioned before, we have chosen E to be the squared ground velocity integrated over the space–time window in which this feature appears most prominently. To isolate the feature, and to permit this measure of basin excitation to give unequal weights to the three directional components of the velocity field, we define a (symmetric, positive semi-definite tensor-valued and dimensionless) windowing function with bounded components $W_{ij}(\mathbf{x},t)$ and define E by

$$E(\mathbf{v}) = \int_0^T \mathrm{d}t \int_{\tilde{\Omega}} \frac{1}{2}\left(\rho_0/T\right)\mathbf{v}\cdot\boldsymbol{W}\cdot\mathbf{v}\,dV, \quad \mathbf{v}\in V. \tag{43}$$

In the examples to be presented, we only use scalar windows, that is, of form $W(\mathbf{x},t)\delta_{ij}$, giving equal weight to all components, and (43) becomes just the mean kinetic energy. We introduce d^* as a shorthand for $DE(\mathbf{v}_0;\cdot)$, and for the special case where E is defined by (43), we have (Appendix B)

$$d^*(\mathbf{w}) = \int_0^T \mathrm{d}t \int_{\tilde{\Omega}} \left(\rho_0/T\right)\mathbf{v}_0\cdot\boldsymbol{W}\cdot\mathbf{w}\,\mathrm{d}V, \quad \forall\mathbf{w}\in V. \tag{44}$$

Then, for future reference, we introduce the adjoint field $\boldsymbol{\psi}_d$ associated with source d^*, which is defined as the solution to

$$\mathcal{A}_0^t\boldsymbol{\psi}_d = d^*. \tag{45}$$

Recalling (33a) we have $\mathcal{A}_0^t = \mathcal{A}_0$, and comparing (44) with (27), we note that

$$d^*(\mathbf{w}) = \mathcal{F}[0,0,0;\ 0,\mathbf{b}_d,0](\mathbf{w}) = \int_{\tilde{\Omega}^T} \mathrm{d}V\ \mathbf{b}_d * \mathbf{w}, \tag{46}$$

where

$$\mathbf{b}_d = \left(\rho_0/T\right)\Pi\left(\mathbf{v}_0\cdot\boldsymbol{W}\right). \tag{47}$$

That is, $\boldsymbol{\psi}_d$ is a solution to (23) with reference values of the density and modulus tensor, and right-hand side term $\mathbf{b}$ set to $\mathbf{b}_d$ as given by (47), that is, proportional to the time reversal of the windowed reference field $\mathbf{v}_0\cdot\boldsymbol{W}$. With the dimensions we have assigned E, $\mathbf{b}_d$ has the dimensions of an applied body-force density, so $\boldsymbol{\psi}_d$ has dimensions of displacement (the fact that the dimensional interpretation of (23) differs from the previous one is irrelevant).

5.2 Adjoint evaluation of source and path sensitivities

Our objective is to calculate $d^*(\delta\mathbf{v}_\chi)$, giving the first-order sensitivity of E to velocity-field perturbations associated with some source or path perturbation. Inverting (42) for $\delta\mathbf{v}_\chi$, we have that

$$d^*\left(\delta\mathbf{v}_\chi\right) = d^*\left(G_0\delta f_\chi^*\right), \tag{48}$$

and by the definition (32) of the transpose,

$$d^*\left(\delta\mathbf{v}_\chi\right) = \delta f_\chi^*\left(G_0^t d^*\right). \tag{49}$$

Finally, inverting (45) to $\boldsymbol{\psi}_d = G_0^t d^*$ and substituting into (49) gives the general result sought,

$$d^*\left(\delta\mathbf{v}_\chi\right) = \delta f_\chi^*\left(\boldsymbol{\psi}_d\right). \tag{50}$$

The right-hand side of (50) gives perturbation $\boldsymbol{d}^*(\delta\mathbf{v}_\chi) \equiv DE\left(\mathbf{v}_0;\delta\mathbf{v}_\chi\right)$ in the form of integrations over the reference field and the adjoint field, so the first-order response of E to a large ensemble of perturbations can be calculated from these two fields by simple quadrature, without additional wavefield simulations.

5.3 Source perturbations

Eq. (50) with subscript $\chi = s$ gives the excitation sensitivity to arbitrary slip-rate perturbation $\delta\dot{\mathbf{s}}$; substituting from (38) for δf_s^* and using (35) and (36) gives

$$d^*(\delta\mathbf{v}_s) = \int_{\Sigma^T} \mathrm{d}A \left[\alpha \left(\hat{\boldsymbol{\upsilon}} \cdot \dot{\boldsymbol{C}}_0 : *\nabla\boldsymbol{\psi}_d\right)^+ + (1-\alpha)\left(\hat{\boldsymbol{\upsilon}} \cdot \dot{\boldsymbol{C}}_0 : *\nabla\boldsymbol{\psi}_d\right)^-\right] * \delta\dot{\mathbf{s}}, \tag{51}$$

and each $\pm$ superscripted factor can be interpreted as a fault-plane traction (positive- and negative-side values, respectively) associated with $\boldsymbol{\psi}_d$. Note that $\boldsymbol{\psi}_d$ satisfies traction continuity on the fault plane. The latter is true by (23d), because (45), with source (46), is equivalent to (23), with all right-hand side terms (and, specifically, the right-hand side of eq. 23d) equal to zero, apart from $\mathbf{b}$. Therefore the factors multiplying α and $1-\alpha$, respectively, are equal and the arbitrary choice of function $\alpha(\mathbf{x})$ introduces no ambiguity in (51). Our example cases will be computed with an isotropic model and $\delta\dot{\mathbf{s}} \cdot \hat{\boldsymbol{\upsilon}} = \mathbf{0}$, in which case (51) reduces to

$$d^*(\delta\mathbf{v}_s) = \int_{\Sigma^T} \mathrm{d}A \left\{\dot{\mu}_0 * \left[\nabla\boldsymbol{\psi}_d + (\nabla\boldsymbol{\psi}_d)^{\mathrm{T}}\right] \cdot \hat{\boldsymbol{\upsilon}}\right\} * \delta\dot{\mathbf{s}}, \tag{52}$$

where $\dot{\mu}_0$ is the distributional time derivative of the unperturbed shear relaxation function, and the right-hand side can be evaluated on either the plus or minus side of the fault plane.

As a means of comparing the effects of specific perturbations to the slip-rate model (e.g. adjusting slip upward by 10 per cent on one fault segment versus making the same adjustment on another segment), eq. (51) is rigorous (albeit only first order), and can be usefully applied to enable many such comparisons for the cost of simple quadratures. Inherent in (51) is that it correctly accounts for phase interference between the reference and perturbed fields.

The latter attribute can instead become a liability when we seek a more synoptic view of the source sensitivity, wherein source changes may be relatively large (admitting, e.g. changes of rupture velocity, reversal of rupture direction or change of rupture length). However, there is an alternative interpretation of (51) that remains useful. Because of the linearity of the equations of motion, eqs (37) and (38) still apply when we interpret $\delta\dot{\mathbf{s}}$, $\delta\mathbf{v}_s$ not as perturbations to the reference fields, but as a complete source and its corresponding velocity field. To obtain the corresponding reinterpretation of $d^*(\delta\mathbf{v}_s)$, we assume that the (complete) source represented by $\delta\dot{\mathbf{s}}$ still excites the propagation feature of interest that we identified in the reference field, so that $\boldsymbol{W} \cdot \delta\mathbf{v}_s(\mathbf{x}, t) \approx k\boldsymbol{W} \cdot \mathbf{v}_0(\mathbf{x}, t+\tau) + \mathbf{v}_u(\mathbf{x}, t)$, where k and τ are some unknown scale factor and time-shift, respectively, and $\mathbf{v}_u$ is a remainder that has negligible correlation with $\mathbf{W} \cdot \mathbf{v}_0$ (this approximation is motivated by the persistence, over diverse southern SAF scenarios, of specific waveguide-like effects, as noted in Section 2). Then, we use (51) to evaluate $d^*[\delta\mathbf{v}_s(\mathbf{x}, t-\tau')]$ repeatedly, adjusting τ' to maximize its absolute value, and we note that (by 44) this maximum (at $\tau' = \tau$) is proportional to excitation factor k associated with source $\delta\dot{\mathbf{s}}$.

5.4 Path perturbations

Eq. 50 with subscript $\chi = C$ gives the sensitivity to modulus variations. Substituting for δf_C^* from (40) and (41), and using the fact that $\boldsymbol{\psi}_d$ is continuous across the fault plane (by the same reasoning as in the last paragraph), we obtain

$$d^*(\delta\mathbf{v}_C) = \delta f_C^*(\boldsymbol{\psi}_d) = -\int_{\hat{\Omega}^T} \mathrm{d}V\, \nabla\boldsymbol{\psi}_d : *\delta\dot{\boldsymbol{C}} : *\nabla\mathbf{v}_0. \tag{53}$$

If only the unrelaxed modulus is perturbed, so that $\delta\dot{\boldsymbol{C}} = \delta\boldsymbol{c}_u(\mathbf{x})\delta(t)$, (53) becomes essentially identical to the expression derived in adjoint tomography for the sensitivity of the misfit function to modulus perturbations, for example Liu & Tromp (2006) (except for the nature of the source terms generating the fields $\mathbf{v}_0$ and $\boldsymbol{\psi}_d$). Following those authors, we can rewrite (53) as

$$d^*(\delta\mathbf{v}_C) = \delta f_C^*(\boldsymbol{\psi}_d) = \int_{\hat{\Omega}} \mathrm{d}V\, \delta\boldsymbol{c}_u :: \boldsymbol{K}_C, \tag{54}$$

where the fourth-order kernel tensor $\boldsymbol{K}_C(\mathbf{x})$ is given by

$$\boldsymbol{K}_C = -\int_0^T \nabla(\Pi\mathbf{v}_0)\nabla\boldsymbol{\psi}_d \mathrm{d}\tau, \tag{55}$$

and the notation in (54) indicates (following Liu & Tromp) contraction on all four indices. For the case of an isotropic medium, we can simplify by decomposing the second-order tensor $\delta\boldsymbol{c}_u : \nabla\boldsymbol{\psi}_d$ into isotropic and deviatoric components, multiplied, respectively, by bulk and shear moduli, κ and μ. This decomposition leads to separate scalar kernels K_κ and K_μ for calculating responses $d^*(\delta\mathbf{v}_\kappa)$ and $d^*(\delta\mathbf{v}_\mu)$ to perturbations in κ_u and μ_u, respectively; and these in turn can be combined to give two scalar-valued kernels K_α and K_β for calculating responses $d^*(\delta\mathbf{v}_\alpha)$ and $d^*(\delta\mathbf{v}_\beta)$ to perturbations to the P and S wave speeds, respectively. These results are all given by Liu & Tromp (2006), and Appendix C summarizes them in the present notation (for consistency with Liu and Tromp, we use subscripts α and β in this paragraph and in Appendix C to refer to the wave speeds; this, of course, differs from our use of α and β in other contexts). In the applications, we use functions $K_\alpha(\mathbf{x})$ and $K_\beta(\mathbf{x})$ to illuminate the predominant propagation wave types and pathways that contribute to the basin excitations under investigation.

5.5 Computation of adjoint field

To obtain the results in the next section, we compute a numerical solution for $\boldsymbol{\psi}_d$ by introducing source term $\mathbf{b}_d(\mathbf{x}, t) = \left(\rho_0/T\right)\mathbf{v}_0(\mathbf{x}, T-t) \cdot \boldsymbol{W}(\mathbf{x}, T-t)$ into the same finite difference code used to compute reference solution $\mathbf{v}_0$, treating the source term the way one would ordinarily treat a body-force density and the adjoint field as though it were a displacement field. Then the bracketed factor in (52) corresponds to what would ordinarily be interpreted in the finite difference code as a fault-resolved shear stress, which we refer to here as the adjoint stress field. We save the adjoint stress field on the fault surface and calculate an ensemble of source-induced perturbations from (52). Likewise, from the same adjoint field we save the displacement gradient $\nabla\boldsymbol{\psi}_d$ and calculate $K_\alpha(\mathbf{x})$ and $K_\beta(\mathbf{x})$ from (55) using Appendix C.

6 APPLICATION TO SAF EARTHQUAKE SCENARIOS

The method described in Section 5 has been applied to analyse the ShakeOut V1.2 scenario (Jones *et al.* 2008) mentioned in Section 2. In that simulation of a M7.8 northeastward-rupturing SAF event in southern California, the LAB and the Ventura basin (VTB) each showed strong excitation, and inspection of the simulations

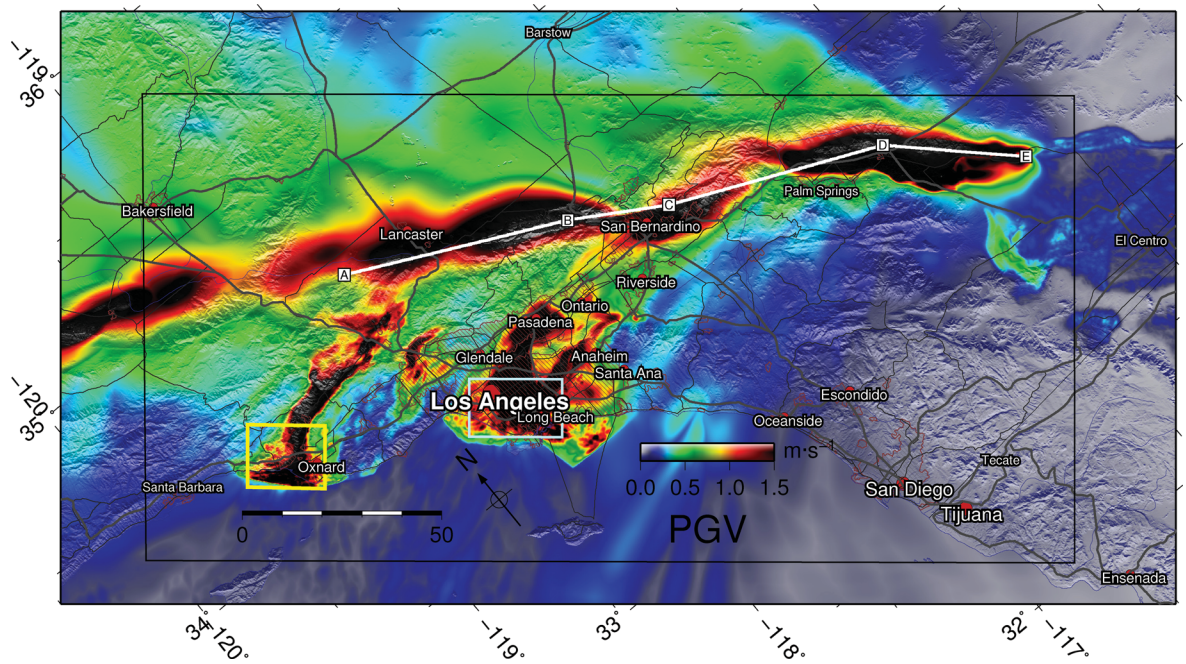

Figure 2. Horizontal peak ground velocities (m s^{-1}) obtained from an elastodynamic simulation of ShakeOut V1.2b. The thick white line along the SAF shows the portion of the fault that ruptured in the scenario. The intersection of the interior of the 1 m s^{-1} PGV contour and the yellow rectangle defines the spatial window for the Ventura Basin excitation functional; the LAB window is similarly defined using the cyan rectangle. The Supporting Information to this paper contains an animation of ground velocities for the elastodynamic simulation (Video S1).

suggests an interpretation in which waveguide-like channelling by sedimentary basins is partly responsible for the high amplitudes.

ShakeOut was calculated using the Southern California Earthquake Center (SCEC) Community Velocity Model (CVM) Version 4 (Magistrale *et al.* 2000; Kohler *et al.* 2003). Fig. 2 shows the horizontal peak ground velocities. We excluded anelastic attenuation from this calculation (in order to have a somewhat simplified test case); had we included anelastic attenuation (as in previous calculations for this scenario by ourselves and other, e.g. Graves *et al.* 2008; Olsen *et al.* 2009; Bielak *et al.* 2010), PGV values in Fig. 2 would have been somewhat lower. In this case, however, the subsequent sensitivity analyses are little affected by the neglect of attenuation (the basin excitations under study having predominant periods of several seconds).

The computational domain of the ShakeOut scenario includes a volume of 600 × 300 × 80 km^3, discretized by 1.8 billion nodes, with a horizontal discretization interval of 200 m. To facilitate the subsequent calculation of the source and path sensitivities (over a range of depth slices), we saved the velocities inside a 200 × 100 × 16 km^3 volume that includes the southern SAF and the western parts of the LAB and VTB (rectangles in Fig. 2) containing high amplitudes. This information allows us to construct the source for the adjoint calculation described in Section 5.5, and provides the reference-field factor for the path kernels (55).

We evaluate the sensitivity of LAB and VTB excitations to perturbations of the fault slip that we parametrize in terms of location and rupture velocity. Each slip-rate perturbation takes the form of a triangular slip pulse of duration 10 s, propagating unilaterally along the local fault strike (either toward northwest or southeast) over a 50-km-fault segment, at a constant velocity. The slip amplitude is tapered with a cosine window in the along-strike direction; amplitude is constant in the upper 8 km, then cosine-tapered between 8 km and 16 km depth. We parametrize the slip perturbation in terms of the segment location (its along-strike centre) and its rupture velocity, in each case selecting the origin-time to maximize $|d^*(\delta \mathbf{v}_s)|$ in order to represent the source sensitivity independently of the potentially random phase-interference between the reference and perturbed fields, as discussed in the final paragraph of Section 5.3.

6.1 Los Angeles basin excitation

To define the LAB excitation functional, we set the window $W(\mathbf{x}, t)$ in (43) to be the product of a spatial window and a temporal window. The spatial window includes the upper grid-cell layer (200 m deep) within the geographical region given by the intersection of (i) the area indicated by the cyan rectangle in Fig. 2 and (ii) the 1 m s^{-1} peak horizontal ground velocity contour of the reference simulation; W is set to zero outside that zone. This definition puts the focus on the origin of high-amplitude excitation in the deepest parts of the Los Angeles basin, which lies some 50 km from the nearest point of the ShakeOut scenario rupture. The temporal factor of window W has the value one from time zero until $t = 176$ s, and then tapers linearly to zero at $t = T = 187$ s. This choice for the time-interval endpoint T corresponds to the time when the dominant surface wave train has reached the southern margin of the Los Angeles basin, as determined from inspection of velocity snapshots of the reference simulation. All velocity time-series in this window were then time-reversed and applied as a body-force density in the adjoint simulation for $\boldsymbol{\psi}_d$, as described in Section 5.5. We saved the adjoint field over a sufficiently large volume to enable (together with the stored reference simulation) the calculation of the path sensitivity kernels (eq. 55 and Appendix C). We also saved the adjoint shear-stress on the fault surface to enable calculation of the source sensitivities via (52) (Video S2 in the Supporting Information to this paper is an animation showing $\dot{\boldsymbol{\psi}}_d$ on the free surface and adjoint shear stresses on the fault).

6.1.1 *Source sensitivity calculations*

Fig. 3 shows the resulting source sensitivity as a function of location along the ShakeOut scenario rupture trace, with each curve representing a particular rupture velocity and rupture direction (solid curves for northwestward rupture, dashed for southeastward). Only relative values are meaningful and sensitivities have been normalized to fit within the zero to one range. The most striking feature of this figure is the extremely great difference between northeastward and southwestward rupture directions. This remarkably strong directivity effect on Los Angeles Basin excitation was first identified by Olsen *et al.* (2006) from a pair of M7.7 simulations, and was seen again in subsequent studies; Fig. 3 confirms that the large directivity effect is present for a wide range of rupture velocities, and applies individually to rupture contributions coming from everywhere on the ShakeOut rupture surface, apart from the northernmost 50 km (where both rupture directions contribute comparable excitation). From here on, therefore, we focus on the northwestward rupture velocities (solid curves). A high-sensitivity zone runs from roughly the Cajon Pass (halfway between points B and C) to the northern Coachella Valley (about halfway between C and D), with the maximum sensitivity just to the SE of bend C. Sensitivity for the southern segment DE is still significant, but about a factor of three lower than the peak near bend C. The northern segment AB yields markedly lower LAB excitation than do other segments, and its contribution decreases rapidly towards the NW end of the ShakeOut rupture. The LAB excitation sensitivity at the peak near bend C is highest for a (northwestward) rupture velocity ∼3250 m s^{-1} and diminishes fairly rapidly for velocities below about 3000 m s^{-1}.

Fig. 4 shows the rupture velocities used to evaluate the source sensitivities, normalized by the shear wave velocity on the fault plane. The ratios are binned into four ranges, distinguishing sub-Rayleigh, super-Rayleigh to subshear, supershear to subsonic and supersonic rupture-velocity categories. For slip located near bend C (the sensitivity peak in Fig. 3), the highest sensitivity is for rupture velocities in the range ∼3000–3500 m s^{-1}. Near bend C, 3000 m s^{-1} falls in the rupture-velocity range (between local Rayleigh and S wave speeds) that is energetically forbidden (asymptotically, for small frictional breakdown zone), and 3500 m s^{-1} is only marginally above the forbidden range. Numerical simulations of dynamic rupture (Ely *et al.* 2010) indicate that, even in complex ruptures undergoing large fluctuations in rupture velocity (for which the asymptotic result is not strictly applicable), there is diminished occurrence of rupture velocities within and near the asymptotically forbidden range, relative to both higher and lower velocities. Thus, it appears that the LAB is most strongly excited by rupture in a velocity range that may be energetically disfavoured. This emphasizes the need for caution in the construction of kinematic source parametrizations (which are typically not constrained by energetic considerations), and the possible benefits of informing those parametrizations with results from spontaneous rupture models (Day *et al.* 2008b; Olsen *et al.* 2008, 2009).

6.1.2 *Comparison with forward simulations*

We compare the foregoing estimates of LAB source sensitivities with results from a set of forward simulations for individual segments of the ShakeOut scenario (in this case including anelastic attenuation), for which peak velocity maps are shown in Fig. 5. Fig. 5(a) is for rupture confined to the northernmost segment, AB, and Fig. 5(b) is for the central segment BD. Segment AB produces very low amplitudes in LAB, less than 25 per cent of those from the BD rupture. This result would have been *a priori* very surprising, since segment AB is on average considerably closer to LAB than is segment BD (and only ∼30 per cent lower in length and seismic moment); yet the result is in good agreement with expectations from the adjoint analysis in Fig. 3 (even though we have made no effort to conform the rupture segments used in the synoptic analysis in Fig. 3 with the specific ruptures used for Fig. 5). Comparing LAB excitation from northernmost rupture AB with that from southernmost rupture DE (Fig. 5c), we again obtain a result that would have been very surprising *a priori*, namely that rupture of DE generates LAB amplitudes more than twice as high as those from AB, even though the latter is far closer to LAB and has rupture length (and moment) almost twice that of DE. And, again, this relationship is consistent with the adjoint-derived sensitivities in Fig. 3.

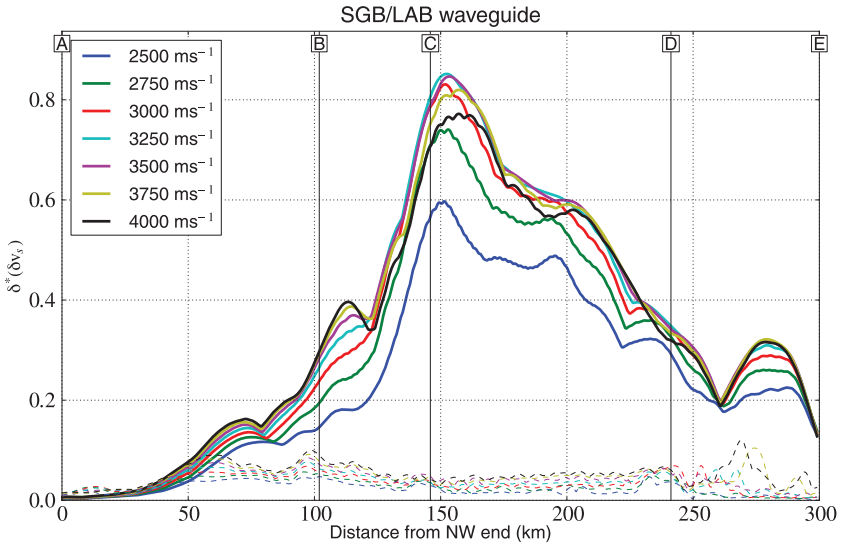

Figure 3. LAB excitation sensitivity (from eq. 52) for slip perturbations to ShakeOut scenario that are parametrized by location (distance along SAF from NW to SE along the SAF) and rupture velocity, as described in text. Curves are solid for rupture from SE to NW, dashed for rupture from NW to SE.

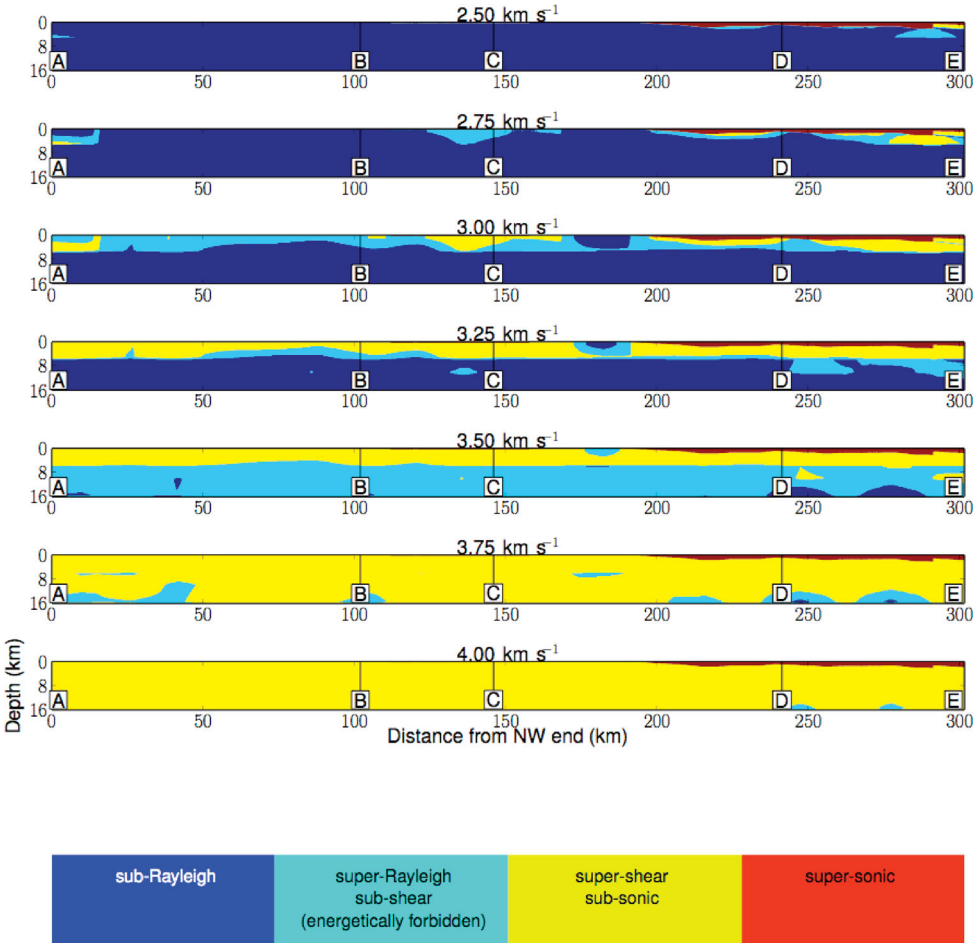

Figure 4. Rupture velocities compared with the speeds of *S*, *P* and Rayleigh waves (the latter approximated by the Poisson solid value of 0.92 times the *S*-wave speed) along the fault.

6.1.3 Path sensitivity kernels

Fig. 6 shows the *P*- and *S*-wave path-sensitivity kernels K_α and K_β, computed from convolutions of the reference- and adjoint-field gradients via (55), specialized to isotropy as in Appendix C. The map views in Figs 6(a) and (b) show horizontal slices of K_α and K_β, respectively, at 1 km depth, while the fence diagrams in Figs 6(d) and (e) contain the cross-sections indicated in the map views. Figs 6(c) and (f) show, in the same format, the SCEC CVM-4 *S*-wave speed distribution. Since these kernels are indices of the sensitivity of the LAB excitation to wave-speed perturbations, they illuminate the predominant pathways of seismic energy entering the basin in the reference scenario. Because the sensitivities are predominantly negative (wave speed increase is associated with reduced excitation), the colour map in Fig. 6 was limited to the negative part of the kernels, and our discussion will be in terms of absolute value (i.e. high sensitivity will mean high $|K_\alpha|$ and/or high $|K_\beta|$).

One pathway delineated by the kernels projects roughly westward from the centre of fault segment BC, along the southern margin of the transverse ranges, following the LAB-San Bernardino cross-section. Inspecting that cross-section, we see that this feature represents a surface wave path. East of the cross-section bend NE of Pasadena, the kernels along this path extend to depths an order of magnitude greater than the depth extent of the sedimentary layers (which are at most a few hundred metres thick there). However, as seen in Fig. 6(c), there is a more deep-seated corridor along the southern margin of the transverse ranges where basement *S* velocity is reduced relative to the transverse ranges to the north and Peninsular Ranges to the south, and this deeper velocity contrast appears to be at least partially responsible for prominence of this pathway in deflecting seismic energy westward from the SAF. Where this cross-section bends west–southwestward near Pasadena, the *S*-wave kernel attains very high amplitude in the SGB (where sediment depth is several kilometres), indicating a strong interaction of the surface wave with the northeastern edge of that basin, which then entrains and funnels surface wave energy into LAB. A careful comparison of the cross-sections reveals that K_β increases abruptly near the point marked Pasadena on the cross-section, without a comparable jump in K_α, suggesting that the basin-edge interaction occurs largely as a conversion to Love waves. This latter part of the path matches the conceptual picture of the SGB acting as a sedimentary waveguide, as suggested by Olsen *et al.* (2006), and the predominance of the *S*-wave kernel is consistent with their identification of this feature as (predominantly) a channelled Love wave (and Ma *et al.* 2007, from direct inspection of simulations, also proposed that the SGB basin-edge induced strong Love-wave conversions). To the east of SGB, the adjoint analysis requires a refinement of the Olsen *et al.* sedimentary-channelling conceptual picture, in that basement structure may be at least as important as the sedimentary layer in

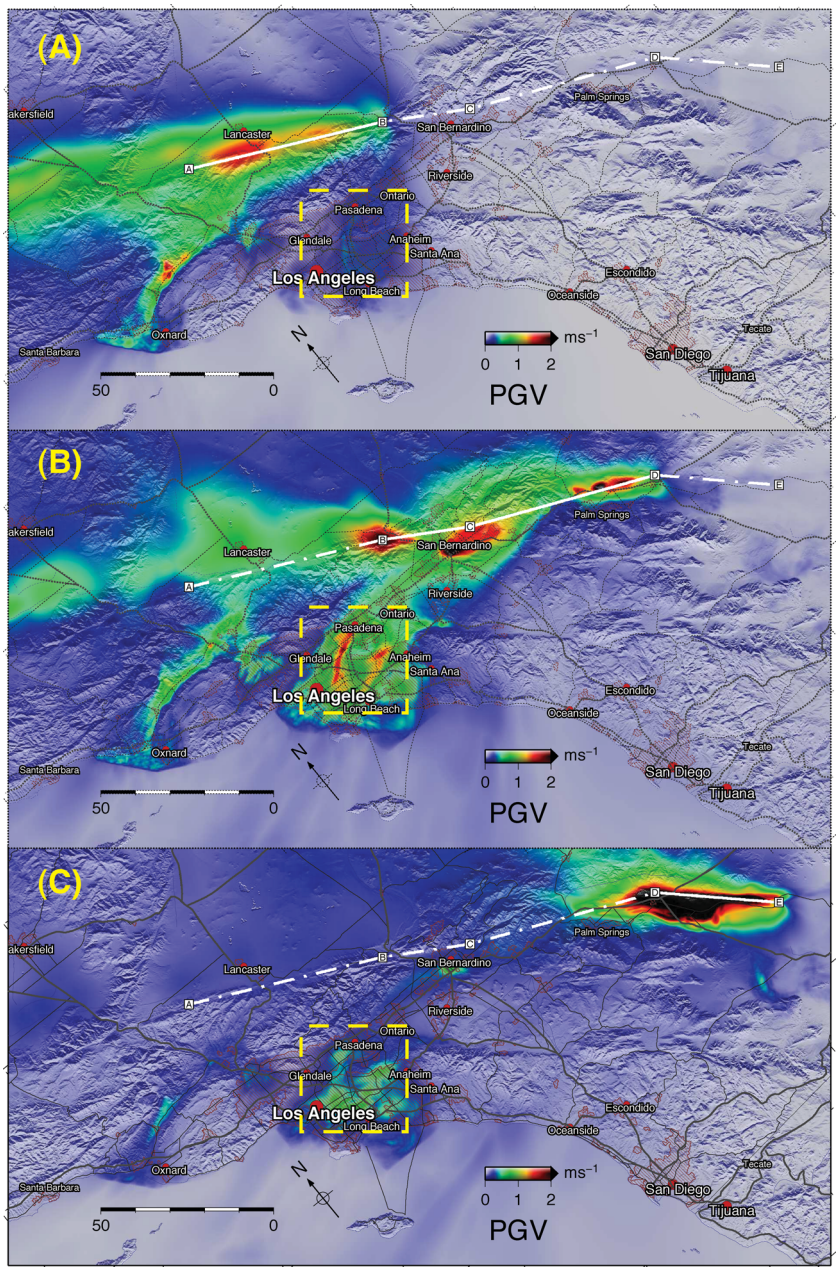

Figure 5. PGVs for partial simulations of the ShakeOut scenario. (a) Northernmost segment AB rupturing alone (maximum PGV in dashed square zone around LAB and SGB is 0.44 m s^{-1}). (b) Central segment BD rupturing alone (maximum PGV in LAB/SGB is 1.9 m s^{-1}). (c) Southernmost segment DE rupturing alone (maximum PGV in LAB/SGB is 0.93 m s^{-1}).

inducing the initial westward deflection of the relatively long-period (4–5 s) surface waves that dominate LAB excitation (in the sense of our mean kinetic energy functional E).

A second, subparallel pathway is evident south of the previous one, and just north of the EW cross-section that terminates in Long Beach. This feature, likewise a surface wave, skirts the northern edge of the Peninsular Ranges near Riverside, then interacts strongly with the eastern edge of the LAB, NE of Anaheim. The two pathways are separated by the Puente and Chino Hills (just NE of the Glendale-Anaheim cross-section) as they enter LAB, and they merge in the very deep, central portion of that basin.

The path kernels are also consistent with the source sensitivities noted above. As they encounter the SAF, the kernels have high amplitude on fault segment BC and on the most northwesterly part of segment CD, consistent with the regions of highest source sensitivity. The low source sensitivity for southwestward rupture is also consistent with the nature of the path kernels: the northwestward propagating forward directivity pulse developed by a northwestward SAF rupture beginning at (or south of) the predominant EW pathways imaged by kernels K_α and K_β is readily deflected through the small angle that those paths make with the SAF. This would not be true for a southeastward rupture, nor for a northwestward rupture beginning north of intersection of those paths with the SAF, and all these inferences are confirmed by the source sensitivity functions in Fig. 3. Finally, note that in both kernels (though a little more evidently in K_α), there is a visible, though very weak, connection

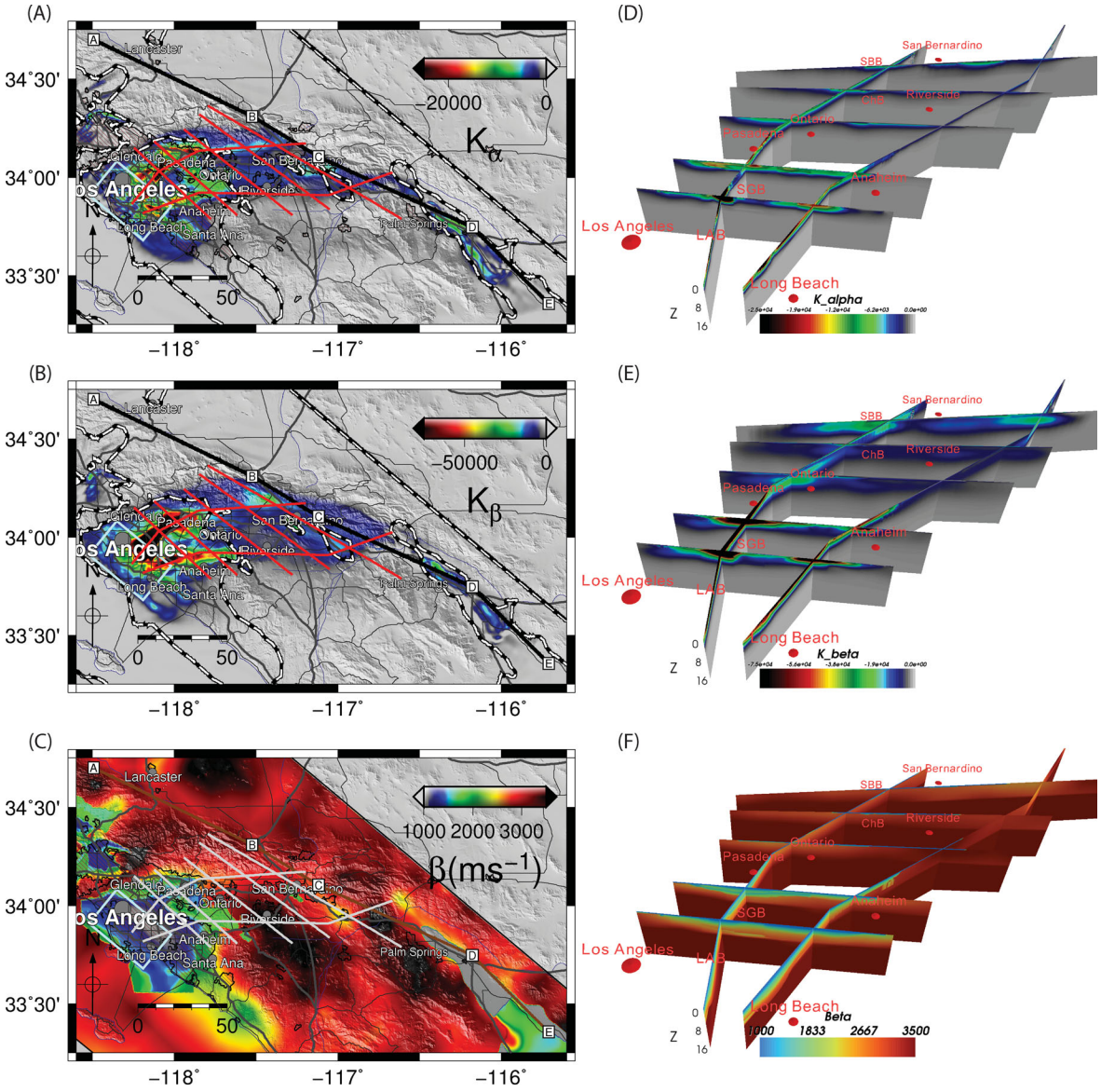

Figure 6. One-kilometre depth slices of the path sensitivity kernel (a) K_α and (b) K_β for LAB, with (c) *S*-wave speed depth slice for comparison. Red lines in (a) and (b) and white lines in (c) show the cross-section locations for the corresponding fence diagrams in (d), (e) and (f), respectively (the Supporting Information to this paper contains Figs 6(a)–(c) in KMZ format for display in Google Earth® or other similar software).

between SAF segment DE and the southern part of LAB near Santa Ana, indicating that a small component of the LAB excitation is induced by waves taking a more direct path and interacting with the SE edge of LAB.

6.2 VTB excitation

We use the same method to explore the origins of the large ground motion generated by the ShakeOut scenario in the VTB. In this case, the excitation functional E was again defined by (43), now with the spatial factor of window W given by the part of the upper grid-cell layer that is both (i) within the urban area around Oxnard (yellow rectangle in Fig. 2) and (ii) experienced reference-simulation PGV exceeding 1 m s^{-1}.

6.2.1 *Source sensitivity kernels*

The source sensitivity analysis is shown in Fig. 7, and it confirms that the Oxnard area excitation of the VTB (which we will refer to simply as the VTB excitation) is most sensitive to northwestward rupture near the centre of SAF segment AB. Southeast of bend C the sensitivity decreases steadily, with the southern segment DE contributing only marginally to the waveguide amplifications. In all segments, sensitivity is very low to southeastward rupture, usually more than an order of magnitude lower than for northwestward rupture. Focusing just on the northwestward-rupture case, sensitivity reaches its highest values, and is nearly invariant, throughout the rupture velocity range 3250–4000 m s^{-1} (the highest we computed), decreasing monotonically for lower rupture velocities. A comparison with the local *S*-wave velocity along the fault (Fig. 4) shows

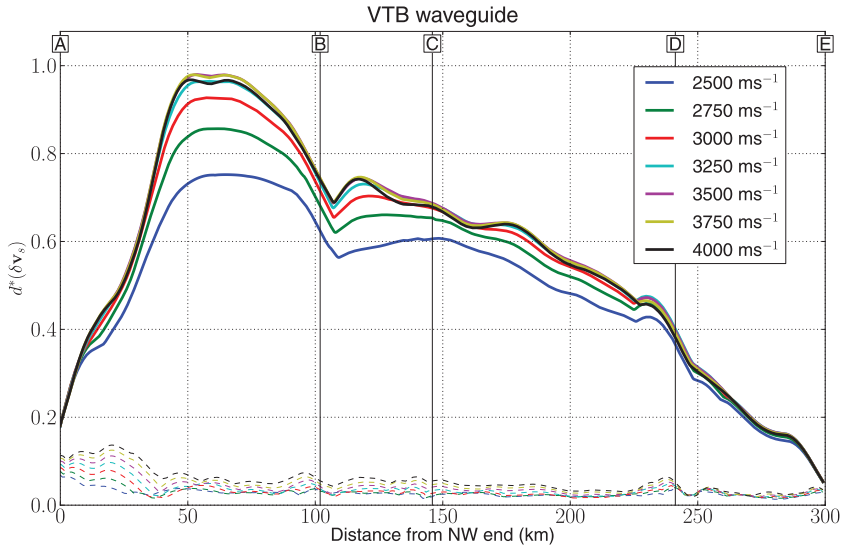

Figure 7. Ventura Basin excitation sensitivity for slip perturbations to ShakeOut scenario that are parametrized by location and rupture velocity, as described in text. Curves are solid for rupture from SE to NW, dashed for rupture from NW to SE.

that the rupture is mostly super-shear for this high-sensitivity range, and sometimes inside the (asymptotically) energetically precluded regime, again suggesting that physical constraints on the source kinematics may reduce unphysical extremes in ground motion predictions.

6.2.2 Path sensitivity analysis

Fig. 8 shows path sensitivities, both in cross-section and as depth slices at 2 km. The dominant feature in map view (Figs 8a and b) is a channel with high *S*-wave sensitivity along the VTB all the way from the coastline to the San Gabriel mountains (near point D on the cross-section map, Fig. 8f). Further east there is a gradual decrease of the *S*-wave kernel, accompanied by a steady increase in the *P*-wave kernel, suggesting that seismic energy is transferred from the fault to the eastern margin of the VTB largely via Rayleigh waves, with substantial mode conversion to Love waves occurring at the basin margin (near point C on the cross-section). This interpretation is reinforced in the cross-sections, where an abrupt increase in the amplitude of the *S*-wave kernel is clear near point C (compared with a much less prominent increase in the *P*-wave kernel). The presence of this EW waveguide-like feature explains the high sensitivity of the VTB excitation to rupture on the northern segment AB of the SAF (Fig. 7).

It is noteworthy that the VTB sensitivity kernels in Fig. 8 are very small in SGB and LAB, even though, taken separately, both the reference simulation (Fig. 2) and the VTB adjoint simulation (not shown) produce very high amplitudes in the SGB and LAB. This confirms that the path sensitivity kernels are indeed revealing the regions sampled by the seismic waves that excite (in this case) the VTB, and are not simply highlighting areas of low impedance.

7. SUMMARY AND CONCLUSIONS

The velocity field of a viscoelastic medium in response to a kinematically defined fault slip satisfies a function-valued operator equation, with the operator equal to its transpose. This formulation (constructed here following Herrera & Bielak 1974) is one way of encoding well-known reciprocal relationships (e.g. Tarantola 1988), and provides a convenient setting for the analysis of the response of a numerically simulated velocity field (the reference field) to perturbations of the fault slip and medium properties. When a prominent feature of that velocity field, such as a basin excitation, is quantified by some (generally non-linear) excitation functional E (time-averaged kinetic energy in our examples), eq. (50) represents the first-order sensitivity of that functional to a slip or wave speed perturbation, in the form of a linear functional acting on the so-called adjoint field. The latter satisfies the same operator equation as the reference field, but with a source given by the Fréchet derivative of E, and a single adjoint simulation permits the evaluation of a large ensemble of perturbations. Representing the source perturbations as localized, propagating slip-rate pulses yield a comprehensive view of the source sensitivity. Despite its different conceptual origin, the analysis leads to calculations analogous to those of adjoint tomography, in particular leading to calculation of spatial functions (kernels K_α and K_β) that image the principal propagation pathways and wave types controlling the excitation functional.

Adjoint analysis of prominent basin excitations visible in the ShakeOut simulation of a $M7.8$ earthquake scenario on the southernmost 300 km of SAF leads to a refined understanding of the origin of these excitations. Excitation of the LAB is extremely sensitive to rupture directivity, with excitation amplitude being about an order of magnitude more sensitive to northwestward rupture than to southeastward rupture. Highest sensitivity is to rupture between roughly the Cajon Pass and the northern Coachella Valley, and to rupture velocities of about 3000 m s^{-1} and above. Much of the high-sensitivity rupture-velocity range lies in or near the energetically disfavoured range between Rayleigh and *S* wave speeds, and spontaneous rupture models might shed valuable light on the relative likelihood of occurrence of the (kinematically defined) scenarios that produce the most extreme LAB excitations. The propagation pathways highlighted by the adjoint analysis are dominated by surface waves—deflected westward onto the corridor between the Transverse and Peninsular Ranges—that become channelled into LAB when they interact, respectively, with (i) the northeastern edge of SGB and (ii) the eastern edge of LAB south of the

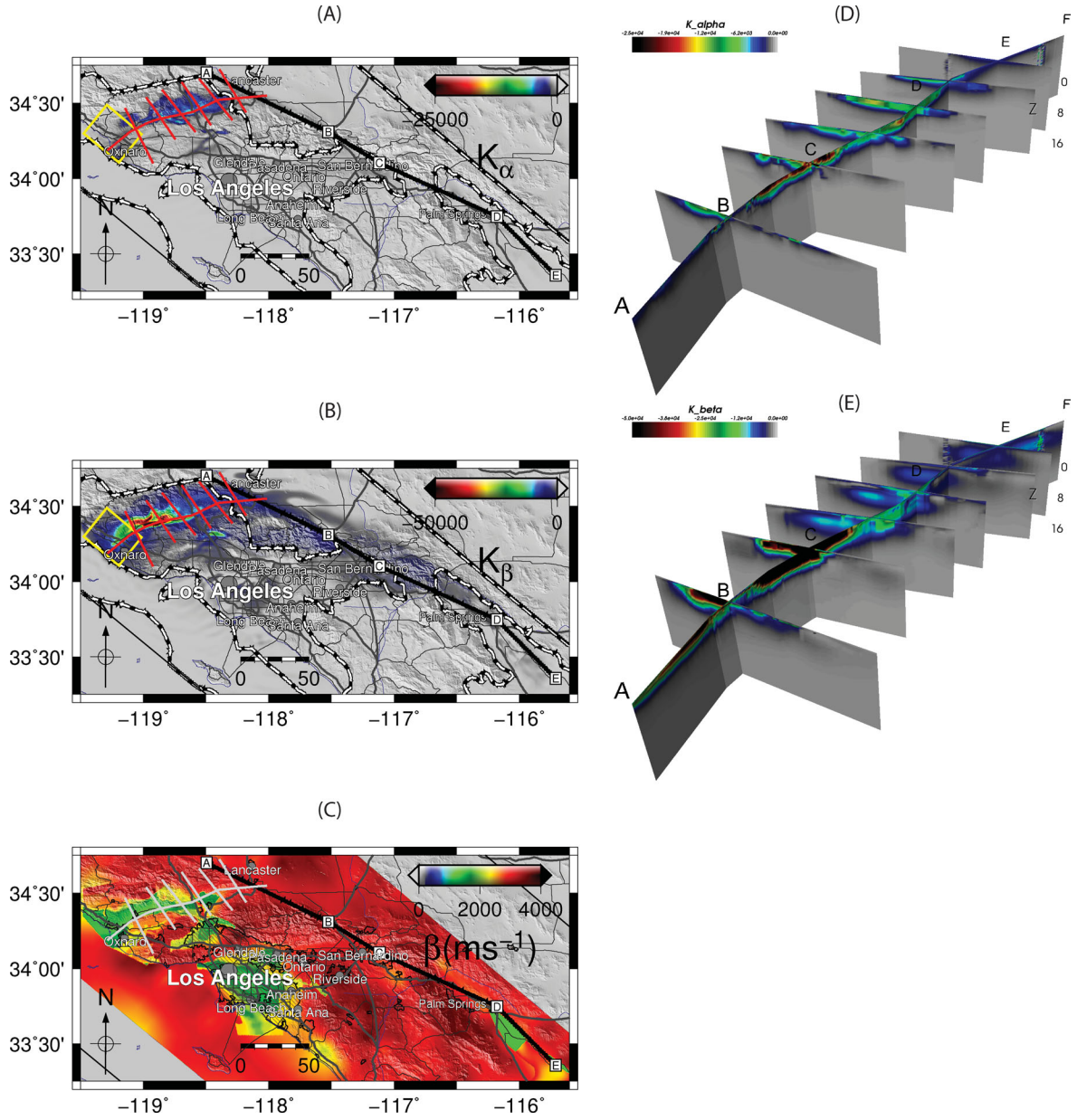

Figure 8. Two-kilometres depth slices of the path sensitivity kernel (a) K_α and (b) K_β for Ventura Basin, with (c) *S*-wave speed depth slice for comparison. Fence diagrams (d) for K_α and (e) for K_β show the indicated cross-sections (the Supporting Information to this paper contains Figs 8(a)–(c) in KMZ format for display in Google Earth® or other similar software).

Chino and Puente Hills. Excitation of the western region of VTB is similarly dominated by the northwestward-propagating directivity pulse, which excites strong Love waves at the eastern margin of the VTB that are then channelled toward the WSW. By illuminating the path and source sensitivities of these large sedimentary-basin excitations, the two adjoint simulations provide a much clearer guide than we would otherwise have for further studies of the seismic hazard and engineering implications of the ShakeOut simulation (and its predecessor SAF scenarios, e.g. Olsen *et al.* 2006, 2008). It is clear, for example, that scenarios with northwestward, supershear rupture and high slip between the transverse ranges and the Coachella Valley will sample the extremes of the probability distribution for LAB excitation from southernmost SAF earthquakes. The analysis also highlights those features of our current models of seismic velocity structure that are most critical for accurate prediction of basin response, and therefore are especially important targets for observational studies (e.g. tomographic inversions such as those of Chen *et al.* 2007; Tape *et al.* 2009).

Similar analysis of numerical simulations may be useful in other environments where complex propagation paths induced by strong lateral gradients in structure produce a first-order effect on seismic hazards. Simulations have revealed substantial waveguide-like effects in accretionary wedges, for example (e.g. Shapiro *et al.* 2000), and these complexities in wave propagation probably lead to similar complexities in the source and path sensitivities of strong motion predictions. It is also straightforward to obtain sensitivities to other parameters not explicitly considered in our examples, such as attenuation parameters. Finally, one could construct other measures of excitation besides the average kinetic energy functional chosen for our examples, the requirement being that the functional possess a

Fréchet derivative, so that the latter can be introduced as the adjoint source in (45).

This type of analysis also has some distinct limitations. It relies on the qualitative, visual identification of wavefield elements having some degree of space–time coherence, as is the case for the basin excitations treated here. We have not explored more systematic approaches to identifying wavefield features for analysis. The adjoint analysis also involves a linearization about the reference solution. More general slip-rate changes can be considered by invoking an alternative interpretation of the Fréchet derivative, at the cost of introducing the ancillary assumptions discussed in Section 5.3. The utility of this latter approach was tested and confirmed for the case of LAB excitation, by comparing forward simulations (Fig. 5) with inferences from the adjoint analysis (i.e. Fig. 3), but we currently have no firm basis from which to define the limits of applicability of the approach.

ACKNOWLEDGMENTS

We thank Jacobo Bielak and an anonymous reviewer for providing helpful reviews. This work was supported by the National Science Foundation (NSF) under grant EAR-0122464, by the Southern California Earthquake Center (SCEC) and by a fellowship for prospective researchers (to DR) from the Swiss National Science Foundation (PBEZ22–117264). SCEC is funded by NSF Cooperative Agreements EAR-0106924 and USGS Cooperative Agreement 02HQAG0008, and NSF awards EAR-074493, EAR-0949443 and OCI-0832698. This is SCEC contribution number 1535.

REFERENCES

Akcelik, V. *et al*., 2003. High resolution forward and inverse earthquake modeling on terasacale computers, in *Proceedings of the 2003 ACM/IEEE Conference for High Performance Computing and Networking,* IEEE Computer Society, Phoenix, Arizona, pp. 8.

Ampuero, J.-P. & Dahlen, F.A., 2005. Ambiguity of the moment tensor, *Bull. seism. Soc. Am.,* **95**, 390–400.

Backus, G. & Mulcahy, M., 1976. Moment tensors and other phenomenological descriptions of seismic sources–II. Discontinuous displacements, *Geophys. J. R. astr. Soc.,* **47,** 301–329.

Bielak, J. *et al*., 2010. The ShakeOut earthquake scenario: verification of three simulation sets, *Geophys. J. Int.,* **180,** 375–404, doi:10.1111/j.1365-246X.2009.04417.x.

Campbell, K.W. & Bozorgnia, Y., 2008. Campbell-Bozorgnia NGA horizontal ground motion model for PGA, PGV, PGD and 5% damped linear elastic response spectra, *Earthq. Spectra,* **24,** 139–171.

Chen, P., Zhao, L. & Jordan, T.H., 2007. Full 3D tomography for crustal structure of the Los Angeles region, *Bull. seism. Soc. Am.,* **97,** 1094–1120, doi:10.1785/0120060222.

Cui, Y. *et al*., 2010. Scalable earthquake simulations on petascale supercomputers, in *Proceedings of the IEEE Supercomputing Conference,* New Orleans, November 2010.

Day, S.M., Graves, R.W., Bielak, J., Dreger, D., Larsen, S., Olsen, K.B., Pitarka, A. & Ramirez-Guzman, L., 2008a. Model for basin effects on long-period response in southern California, *Earthq. Spectra,* **24,** 257–277.

Day, S.M., Gonzalez, S.H., Anooshehpoor, R. & Brune, J.N., 2008b. Scale-model and numerical simulations of near-fault seismic directivity, *Bull. seism. Soc. Am.,* **98,** 1186–1206, doi:10.1785/0120070190.

Edelstein, W.S. & Gurtin, M.E., 1964. Uniqueness theorems in the linear dynamic theory of anisotropic viscoelastic solids, *Arch. Ration. Mech. Anal.,* **17,** 47–60.

Ely, G., Day, S.M. & Minster, J.-B., 2010. Dynamic rupture models for the southern San Andreas fault, *Bull. seism. Soc. Am.,* **100,** 131–150.

Frankel, A. & Vidale, J., 1992. A three-dimensional simulation of seismic waves in the Santa Clara Valley, California, from a Loma Prieta aftershock, *Bull. seism. Soc. Am.,* **82,** 2045–2074.

Graves, R.W., Pitarka, A. & Somerville, P.G., 1998. Ground-motion amplification in the Santa Monica area: effects of shallow basin-edge structure, *Bull. seism. Soc. Am.,* **88,** 1224–1242.

Graves, R., Aagaard, B., Hudnut, K., Star, L., Stewart, J. & Jordan, T.H., 2008. Broadband simulations for *M*w 7.8 southern San Andreas earthquakes: ground motion sensitivity to rupture speed, *Geophys. Res. Lett.,* **35,** L22302, doi:10.1029/2008GL035750.

Graves, R. *et al*., 2010. CyberShake: a physics-based seismic hazard model for southern California, *Pure appl. Geophys.,* **168,** doi:10.1007/s00024-010-0161-6.

Gurtin, M.E., 1964. Variational principles for linear elastodynamics, *Arch. Ration. Mech. Anal.,* **16,** 34–50.

Gurtin, M.E. & Sternberg, E., 1963. On the linear theory of viscoelasticity, *Arch. Ration. Mech. Anal.,* **11,** 291–356.

Heaton, T.H. & Heaton, R.E., 1989. Static deformations from point forces and force couples located in welded elastic Poissonian halfspaces: implications for seismic moment tensors, *Bull. seism. Soc. Am.,* **79,** 813–841.

Herrera, I. & Bielak, J., 1974. A simplified version of Gurtin's variational principle, *Arch. Ration. Mech. Anal.,* **53,** 131–149.

Herrera, I. & Bielak, J., 1977. Comments on the paper "Modified Gurtin's variational principles in the linear dynamic theory of viscoelasticity," *Int. J. Solids Struct.,* **13,** 377–378.

Jones, L.M. *et al*., 2008. The ShakeOut scenario. Open-File Rep 2008–1150, U.S. Geol. Surv.

Kohler, M., Magistrale, H. & Clayton, R., 2003. Mantle heterogeneities and the SCEC three-dimensional seismic velocity model version 3, *Bull. seism. Soc. Am.,* **93,** 757–774.

Komatitsch, D., Liu, Q., Tromp, J., Suss, P., Stidham, C. & Shaw, J.H., 2004. Simulations of ground motion in the Los Angeles basin based upon the spectral-element method, *Bull. seism. Soc. Am.,* **94,** 187–206.

Krishnan, S., Ji, C., Komatitsch, D. & Tromp, J., 2006a. Performance of two 18-story steel moment-frame buildings in southern California during two large simulated San Andreas earthquakes, *Earthq. Spectra,* **22,** 1035–1061.

Krishnan, S., Ji, C., Komatitsch, D. & Tromp, J., 2006b. Case studies of damage to tall steel moment-frame buildings in southern California during large San Andreas earthquakes, *Bull. seism. Soc. Am.,* **96,** 1523–1537.

Leitman, M.J., 1966. Variational principles in the linear dynamic theory of viscoelasticity, *Q. appl. Math.,* **24,** 37–46.

Liu, Q. & Tromp, J., 2006. Finite-frequency kernels based on adjoint methods, *Bull. seism. Soc. Am.,* **96,** 2383–2397.

Luenberger, D.G., 1969. *Optimization by Vector Space Methods,* John Wiley and Sons, New York, NY, 326 pp.

Ma, S., Archuleta, R.J. & Page, M.T., 2007. Effects of large-scale surface topography on ground motions, as demonstrated by a study of the San Gabriel Mountains, Los Angeles, California, *Bull. seism. Soc. Am.,* **97,** 2066–2079, doi:10.1785/0120070040.

Magistrale, H., Day, S.M., Clayton, R. & Graves, R.W., 2000. The SCEC southern California reference three-dimensional seismic velocity model version 2, *Bull. seism. Soc. Am.,* **90,** S65–S76.

Muto, M. & Krishnan, S., 2011. Hope for the best, prepare for the worst: response of tall steel buildings to the ShakeOut scenario earthquake, *Earthq. Spectra,* **27,** 375–398.

Nowick, A.S. & Berry, B.S., 1972. *Anelastic Relaxation in Crystalline Solids,* Academic Press, New York.

Olsen, K.B., 2000. Site amplification in the Los Angeles basin from three-dimensional modeling of ground motion, *Bull. seism. Soc. Am.,* **90,** S77–S94.

Olsen, K.B., Archuleta, R.J. & Matarese, J.R., 1995. Three-dimensional simulation of a magnitude 7.75 earthquake on the San Andreas fault in southern California, *Science,* **270,** 1628–1632.

Olsen, K.B., Day, S.M., Minster, J-B., Cui, Y., Chourasia, A., Faerman, M., Moore, R., Maechling, P. & Jordan, T.H., 2006. Strong shaking in Los Angeles expected from southern San Andreas earthquake, *Geophys. Res. Lett.,* **33,** L07305, doi:10.1029/2005GL025472.

Olsen K.B., Day, S.M., Minster, J-B., Cui, Y., Chourasia, A., Okaya, D., Maechling, P. & Jordan, T.H., 2008. TeraShake2: simulation of Mw7.7 earthquakes on the southern San Andreas fault with spontaneous rupture description, *Bull. seism. Soc. Am.,* **98,** 1162–1185, doi:10.1785/0120070148.

Olsen, K.B. *et al*., 2009. ShakeOut-D: ground motion estimates using an ensemble of large earthquakes on the southern San Andreas fault with spontaneous rupture propagation, *Geophys. Res. Lett.,* **36,** L04303, doi:10.1029/2008GL036832.

Pitarka, A., Irikura, K., Iwata, T. & Sekiguchi, H., 1998. Three dimensional simulation of the near fault ground motion for the 1995 Hyogoken Nanbu (Kobe), Japan earthquake, *Bull seism. Soc. Am.,* **88,** 428–440.

Renardy, M. & Rogers, R.C., 2004. *An Introduction to Partial Differential Equations,* Springer-Verlag, New York.

Shapiro, N.M., Olsen, K.B. & Singh, S.K., 2000. Wave-guide effects in subduction zones: evidence from three-dimensional modeling, *Geophys. Res. Lett.,* **27,** 433–436.

Sieh, K.E. & Williams, P.L., 1990. Behavior of the southernmost San Andreas fault during the past 300 years, *J. geophys. Res.,* **95,** 6629–6645.

Suss, M.P. & Shaw, J.H., 2003. P-wave seismic velocity structure derived from sonic logs and industry reflection data in the Los Angeles basin, California, *J. geophys. Res.,* **108,** 2170, doi:10.1029/2001JB001628.

Tape, C., Liu, Q., Maggi, A. & Tromp, J., 2009. Adjoint tomography of the Southern California crust, *Science,* **325,** 988–992.

Tarantola, A., 1988. Theoretical background for the inversion of seismic waveforms, including elasticity and attenuation, *Pageoph,* **128,** 365–399.

Tromp, J., Tape, C.H. & Liu, Q., 2005. Seismic tomography, adjoint methods, time reversal, and banana-doughnut kernels, *Geophys. J. Int.,* **160,** 195–216.

Weldon, R., Fumal, T.E., Biasi, G.P. & Scharer, K.M., 2005. Past and future earthquakes on the San Andreas Fault, *Science,* **308,** 966–967.

Working Group on California Earthquake Probabilities, 2008. The uniform California earthquake rupture forecast, Version 2 (UCERF 2), Tech. Rep. USGS OFR-2007–1437, CGS SR-203, SCEC C-1138, U.S. Geological Survey in cooperation with the California Geological Survey and the Southern California Earthquake Center.

APPENDIX A: DERIVATION OF $a(\mathbf{v}, \mathbf{w})$ AND f^*.

Letting $(X_j, j = 0, \ldots, 5)$ serve as shorthand for $(H, B_1, B_2, B_2, B_3, B_3)$, which are Hilbert spaces containing, respectively, the ranges of the left-hand sides of the six governing equations (23a–f), we define six corresponding linear operators κ_j, $j = 0, ..., 5$, such that $\kappa_j : V \to X_j$ (e.g. $\kappa_0 : V \to H$, $\kappa_1 : V \to B_1$, etc). Then, for $\mathbf{w} \in V$, form inner products of each of (23a–f) with the corresponding function $\kappa_j \mathbf{w}$. The result is to transform (23) into

$$\mathcal{K}_j \mathbf{v} = f_j^*, \quad j = 0, ..., 5, \tag{A1a-f}$$

which (for the sake of concision) has been expressed in terms of linear operators $\mathcal{K}_j : V \to V^*$ defined by

$$\mathcal{K}_0 \mathbf{v}(\mathbf{w}) = (\mathcal{L}\mathbf{v}, \kappa_0 \mathbf{w})_H , \tag{A2a}$$

$$\mathcal{K}_1 \mathbf{v}(\mathbf{w}) \equiv (\beta_1 \mathbf{v}, \kappa_1 \mathbf{w})_{B_1} , \tag{A2b}$$

$$\mathcal{K}_2 \mathbf{v}(\mathbf{w}) \equiv \left(\gamma_2^{\Delta} \mathbf{v}, \kappa_2 \mathbf{w}\right)_{B_2} , \tag{A2c}$$

$$\mathcal{K}_3 \mathbf{v}(\mathbf{w}) \equiv \left(\beta_2^{\Delta} \mathbf{v}, \kappa_3 \mathbf{w}\right)_{B_2} , \tag{A2d}$$

$$\mathcal{K}_4 \mathbf{v}(\mathbf{w}) \equiv \left(\gamma_3^{I} \mathbf{v}, \kappa_4 \mathbf{w}\right)_{B_3} , \tag{A2e}$$

$$\mathcal{K}_5 \mathbf{v}(\mathbf{w}) \equiv \left(\beta_3^{I} \mathbf{v}, \kappa_5 \mathbf{w}\right)_{B_3} ; \tag{A2f}$$

and functionals f_j^* containing the loads, boundary conditions and initial state,

$$f_0^*(\mathbf{w}) = \left(\left(-\nabla \cdot \boldsymbol{p} + \mathbf{b} + \nabla \cdot \dot{\boldsymbol{T}}^{>}\right), \kappa_0 \mathbf{w}\right)_H , \tag{A3a}$$

$$f_1^*(\mathbf{w}) = \left(\mathbf{p}_n - \dot{\mathbf{T}}_n^{>}, \kappa_1 \mathbf{w}\right)_{B_1} , \tag{A3b}$$

$$f_2^*(\mathbf{w}) = (\dot{\mathbf{s}}, \kappa_2 \mathbf{w})_{B_2} , \tag{A3c}$$

$$f_3^*(\mathbf{w}) = \left(\left(\Delta \mathbf{p}_{\upsilon} - \Delta \dot{\mathbf{T}}_{\upsilon}^{>}\right), \kappa_3 \mathbf{w}\right)_{B_2} , \tag{A3d}$$

$$f_4^*(\mathbf{w}) = (\mathbf{v}_{init}, \kappa_4 \mathbf{w})_{B_3} , \tag{A3e}$$

$$f_5^*(\mathbf{w}) = (\rho \mathbf{a}_{init}, \kappa_5 \mathbf{w})_{B_3} \tag{A3f}$$

(the usage in this Appendix of the notation f_0^* for the volume-integral contribution to the source functional f^* is distinct from its usage elsewhere to indicate the source functional for the reference simulation).

The subspace $V_0 \subset V$ denotes all $\mathbf{w} \in V$ such that the support of $\mathbf{w}$ is disjoint to the space–time boundaries Γ_1, Γ_2, $\Gamma_3 \times \{0\}$ and $\Gamma_3 \times \{T\}$ of R. For $j = 1, ..., 5$, respectively, $V_j \subset V$ will denote the intersection of the null spaces of the four κ_k $k \neq j$. We stipulate that κ_j be such that

$\kappa_j|_{V_j}$ (that is, the restriction of κ_j to V_j) has range dense in X_j, implying that the orthogonal complement of $Rg(\kappa_j|_{V_j})$ in X_j is empty, and that therefore inner product $(\mathbf{v}, \kappa_j \mathbf{w})_{X_j}$ is zero for all $\mathbf{w} \in V_j$ if and only if $\mathbf{v} = 0$; we also require the κ_j to be such that $V_0 \subseteq V_1 \cap V_2 \cap V_3 \cap V_4 \cap V_5$ (i.e. any function with support disjunct to the space–time boundaries must be in the null space of all κ_j, $j = 1, ..., 5$). With these stipulations, the sum of these six inner products satisfies criteria (i) and (ii) of the first paragraph of Section 4.2, so that

$$a(\mathbf{v}, \mathbf{w}) - f^*(\mathbf{w}) = 0, \tag{A4a}$$

with

$$a(\mathbf{v}, \mathbf{w}) \equiv \sum_{j=0}^{5} \mathcal{K}_j \mathbf{v}(\mathbf{w}), \tag{A4b}$$

and

$$f^* \equiv \sum_{j=0}^{5} f_j^*, \tag{A4c}$$

is equivalent to governing eqs (23). Property (i) is obviously satisfied, by construction, and we now demonstrate property (ii), assuming provisionally that the κ_j satisfy the dense range condition stated above. Subsequently we will impose property (iii) of Section 4.2 (symmetry of a) by an appropriate selection of the mappings κ_j, and then verify that they satisfy the dense range condition.

To demonstrate that property (ii) holds, we first note (via the divergence theorem and integration by parts on the left-hand side of eq. A.2a) that

$$\begin{aligned}\mathcal{K}_0 \mathbf{v}(\mathbf{w}) = \tilde{a}(\mathbf{v}, \mathbf{w}) - \mathcal{B}_1 \mathbf{v}(\gamma_1 \circ \kappa_0 \mathbf{w}) + \mathcal{B}_2^{\Delta} \mathbf{v}\left(\gamma_2^{1-\alpha} \circ \kappa_0 \mathbf{w}\right) \\ + \mathcal{B}_2^{\alpha} \mathbf{v}\left(\gamma_2^{\Delta} \circ \kappa_0 \mathbf{w}\right) + \mathcal{B}_3^{F} \mathbf{v}\left(\gamma_3^{F} \circ \kappa_0 \mathbf{w}\right) - \mathcal{B}_3^{I} \mathbf{v}\left(\gamma_3^{I} \circ \kappa_0 \mathbf{w}\right)\end{aligned}, \tag{A5}$$

where $\tilde{a}$ incorporates the integrations on R,

$$\tilde{a}(\mathbf{v}, \mathbf{w}) \equiv -(\rho \dot{\mathbf{v}}, \kappa_0 \dot{\mathbf{w}})_H + \left[\dot{C} : *\nabla \mathbf{v}, \nabla(\kappa_0 \mathbf{w})\right]_{H \otimes H}, \tag{A6}$$

and the each of the following operators maps V into B_1^*, B_2^* or B_3^*,

$$\mathcal{B}_1 \mathbf{v} \equiv (\beta_1 \mathbf{v}, \cdot)_{B_1}, \tag{A7a}$$

$$\mathcal{B}_2^{\Delta} \mathbf{v} \equiv \left(\beta_2^{\Delta} \mathbf{v}, \cdot\right)_{B_2}, \tag{A7b}$$

$$\mathcal{B}_2^{\alpha} \mathbf{v} \equiv \left(\beta_2^{\alpha} \mathbf{v}, \cdot\right)_{B_2}, \tag{A7c}$$

$$\mathcal{B}_3^{F} \mathbf{v} \equiv \left(\beta_3^{F} \mathbf{v}, \cdot\right)_{B_3}, \tag{A7d}$$

$$\mathcal{B}_3^{I} \mathbf{v} \equiv \left(\beta_3^{I} \mathbf{v}, \cdot\right)_{B_3}, \tag{A7e}$$

By similar transformation of (A3a), $f_0^*(\mathbf{w})$ can be written as

$$\begin{aligned}f_0^*(\mathbf{w}) = \left[\boldsymbol{p} - \dot{\boldsymbol{T}}^{>}, \nabla(\kappa_0 \mathbf{w})\right]_{H \otimes H} + (\mathbf{b}, \kappa_0 \mathbf{w})_H \\ - \left(\mathbf{p}_n - \dot{\mathbf{T}}_n^{>}, \gamma_1 \circ \kappa_0 \mathbf{w}\right)_{B_1} + \left(\Delta \mathbf{p}_{\upsilon} - \Delta \dot{\mathbf{T}}_{\upsilon}^{>}, \gamma_2^{1-\alpha} \circ \kappa_0 \mathbf{w}\right)_{B_2}\end{aligned}, \tag{A8}$$

For $\mathbf{w} \in V_0$, (A4a) reduces to

$$\mathcal{K}_0 \mathbf{v}(\mathbf{w}) = f_0^*(\mathbf{w}), \ \mathbf{w} \in V_0, \quad \mathbf{v} \in V, \tag{A9a}$$

which, with definitions (A2a) and (A3a), is

$$(\mathcal{L}\mathbf{v}, \kappa_0 \mathbf{w})_H = \left(\left(-\nabla \cdot \boldsymbol{p} + \mathbf{b} + \nabla \cdot \dot{\boldsymbol{T}}^{>}\right), \kappa_0 \mathbf{w}\right)_H, \quad \mathbf{w} \in V_0, \ \mathbf{v} \in V, \tag{A9b}$$

from which it follows that (23a) is satisfied on every open set in R whose closure excludes the boundary. Because V_0 is dense in H, the orthogonal complement (in H) of V_0 is empty. Therefore (A9) can be extended to all $\mathbf{w} \in V$, so we conclude that

$$\mathcal{K}_0 \mathbf{v}(\mathbf{w}) = f_0^*(\mathbf{w}) \text{ for all } \mathbf{w} \in V, \ \mathbf{v} \in V. \tag{A10}$$

For $\mathbf{w} \in V_j$, (A4a) reduces to

$$\mathcal{K}_0 \mathbf{v}(\mathbf{w}) + \mathcal{K}_j \mathbf{v}(\mathbf{w}) = f_0^*(\mathbf{w}) + f_j^*(\mathbf{w}), \quad \mathbf{w} \in V_j, \mathbf{v} \in V, \qquad j = 1, ..., 5, \tag{A11a-e}$$

which, with (A10), implies

$$\mathcal{K}_j \mathbf{v}(\mathbf{w}) = f_j^*(\mathbf{w}), \quad \mathbf{w} \in V_j, \mathbf{v} \in V, \qquad j = 1, ..., 5. \tag{A12a-e}$$

Therefore, for each j, the corresponding boundary condition in (23) is satisfied ($j = 1, ..., 5$ corresponding, respectively, to 23b–f), showing that property (ii) holds for (A4).

We now impose the symmetry property (iii). Since $a(\mathbf{v}, \mathbf{w}) = \tilde{a}(\mathbf{v}, \mathbf{w})$ for $\mathbf{v}, \mathbf{w} \in V_0$, symmetry of $\tilde{a}$ is a necessary condition for symmetry of a, and from (A6a) we can see (because $C_{ijpq} = C_{pqij}$) that $\tilde{a}$ is symmetric if we specify κ_0 to be the time-reversal mapping Π,

$$\kappa_0 \mathbf{w}(\mathbf{x}, t) = \Pi \mathbf{w}(\mathbf{x}, t) \equiv \mathbf{w}(\mathbf{x}, T - t). \tag{A13}$$

Then (A4b) and (A5), for $\mathbf{w} \in V_j$, $j = 1, ..., 5$, give

$$a(\mathbf{v}, \mathbf{w}) - \tilde{a}(\mathbf{v}, \mathbf{w}) = -\mathcal{B}_1 \mathbf{v}(\gamma_1 \circ \Pi \mathbf{w}) + \mathcal{K}_1 \mathbf{v}(\mathbf{w}), \quad \mathbf{w} \in V_1, \mathbf{v} \in V, \tag{A14a}$$

$$\begin{aligned} a(\mathbf{v}, \mathbf{w}) - \tilde{a}(\mathbf{v}, \mathbf{w}) &= \mathcal{B}_2^{\Delta} \mathbf{v}\left(\gamma_2^{1-\alpha} \circ \Pi \mathbf{w}\right) + \mathcal{B}_2^{\alpha} \mathbf{v}\left(\gamma_2^{\Delta} \circ \Pi \mathbf{w}\right) \\ &\quad + \mathcal{K}_2 \mathbf{v}(\mathbf{w}) + \mathcal{K}_3 \mathbf{v}(\mathbf{w}), \quad \mathbf{w} \in V_2 \cup V_3, \ \mathbf{v} \in V, \end{aligned} \tag{A14b}$$

$$\begin{aligned} a(\mathbf{v}, \mathbf{w}) - \tilde{a}(\mathbf{v}, \mathbf{w}) &= \mathcal{B}_3^{F} \mathbf{v}\left(\gamma_3^{F} \circ \kappa_0 \mathbf{w}\right) - \mathcal{B}_3^{I} \mathbf{v}\left(\gamma_3^{I} \circ \Pi \mathbf{w}\right) \\ &\quad + \mathcal{K}_4 \mathbf{v}(\mathbf{w}) + \mathcal{K}_5 \mathbf{v}(\mathbf{w}), \quad \mathbf{w} \in V_4 \cup V_5, \mathbf{v} \in V. \end{aligned} \tag{A14c}$$

By substituting into (A14) from definitions (A2) and (A7), we get

$$a(\mathbf{v}, \mathbf{w}) - \tilde{a}(\mathbf{v}, \mathbf{w}) = -\left(\beta_1 \mathbf{v}, \gamma_1 \circ \Pi \mathbf{w}\right)_{B_1} + \left(\beta_1 \mathbf{v}, \kappa_1 \mathbf{w}\right)_{B_1}, \quad \mathbf{w} \in V_1, \mathbf{v} \in V, \tag{A15a}$$

$$\begin{aligned} a(\mathbf{v}, \mathbf{w}) - \tilde{a}(\mathbf{v}, \mathbf{w}) &= \left(\beta_2^{\Delta} \mathbf{v}, \gamma_2^{1-\alpha} \circ \Pi \mathbf{w}\right)_{B_2} + \left(\beta_2^{\alpha} \mathbf{v}, \gamma_2^{\Delta} \circ \Pi \mathbf{w}\right)_{B_2} \\ &\quad + \left(\gamma_2^{\Delta} \mathbf{v}, \kappa_2 \mathbf{w}\right)_{B_2} + \left(\beta_2^{\Delta} \mathbf{v}, \kappa_3 \mathbf{w}\right)_{B_2}, \quad \mathbf{w} \in V_2 \cup V_3, \mathbf{v} \in V, \end{aligned} \tag{A15b}$$

$$\begin{aligned} a(\mathbf{v}, \mathbf{w}) - \tilde{a}(\mathbf{v}, \mathbf{w}) &= \left(\beta_3^{F} \mathbf{v}, \gamma_3^{F} \circ \Pi \mathbf{w}\right)_{B_3} - \left(\beta_3^{I} \mathbf{v}, \gamma_3^{I} \circ \Pi \mathbf{w}\right)_{B_3} \\ &\quad + \left(\gamma_3^{I} \mathbf{v}, \kappa_4 \mathbf{w}\right)_{B_3} + \left(\beta_3^{I} \mathbf{v}, \kappa_5 \mathbf{w}\right)_{B_3}, \quad \mathbf{w} \in V_4 \cup V_5, \mathbf{v} \in V. \end{aligned} \tag{A15c}$$

Obviously, the required symmetry is achieved if we chose κ_j, $j = 1, \ldots, 5$, to be

$$\kappa_1 \mathbf{w} = \gamma_1 \circ \Pi \mathbf{w}, \tag{A16a}$$

$$\kappa_2 \mathbf{w} = \beta_2^{\alpha} \circ \Pi \mathbf{w}, \tag{A16b}$$

$$\kappa_3 \mathbf{w} = -\gamma_2^{1-\alpha} \circ \Pi \mathbf{w}, \tag{A16c}$$

$$\kappa_4 \mathbf{w} = -\beta_3^{I} \circ \Pi \mathbf{w} = \beta_3^{F} \mathbf{w}, \tag{A16d}$$

$$\kappa_5 \mathbf{w} = \gamma_3^{I} \circ \Pi \mathbf{w} = \gamma_3^{F} \mathbf{w}, \tag{A16e}$$

which can also be expressed by specifying

$$\mathcal{K}_1 \mathbf{v}(\mathbf{w}) = \mathcal{B}_1 \mathbf{v}(\gamma_1 \circ \Pi \mathbf{w}), \tag{A17a}$$

$$\mathcal{K}_2 \mathbf{v}(\mathbf{w}) = \mathcal{B}_2^{\alpha} \mathbf{w}\left(\gamma_2^{\Delta} \circ \Pi \mathbf{v}\right), \tag{A17b}$$

$$\mathcal{K}_3 \mathbf{v}(\mathbf{w}) = -\mathcal{B}_2^{\Delta} \mathbf{v}\left(\gamma_2^{1-\alpha} \circ \Pi \mathbf{w}\right), \tag{A17c}$$

$$\mathcal{K}_4 \mathbf{v}(\mathbf{w}) = \mathcal{B}_3^{F} \mathbf{w}\left(\gamma_3^{F} \circ \Pi \mathbf{v}\right) = \mathcal{B}_3^{F} \mathbf{w}\left(\gamma_3^{I} \mathbf{v}\right), \tag{A17d}$$

$$\mathcal{K}_5 \mathbf{v}(\mathbf{w}) = \mathcal{B}_3^{I} \mathbf{v}\left(\gamma_3^{I} \circ \Pi \mathbf{w}\right) = \mathcal{B}_3^{I} \mathbf{v}\left(\gamma_3^{F} \mathbf{w}\right). \tag{A17e}$$

From (A4b), (A5), (A7) and (A17), we obtain

$$\begin{aligned} a(\mathbf{v}, \mathbf{w}) &= -\left(\rho \dot{\mathbf{v}}, \kappa_0 \dot{\mathbf{w}}\right)_H + \left[\dot{\mathbf{C}} : *\nabla \mathbf{v}, \nabla(\Pi \mathbf{w})\right]_{H \otimes H} \\ &\quad + \left(\beta_2^{\alpha} \mathbf{v}, \gamma_2^{\Delta} \circ \Pi \mathbf{w}\right)_{B_2} + \left(\beta_2^{\alpha} \mathbf{w}, \gamma_2^{\Delta} \circ \Pi \mathbf{v}\right)_{B_2} + \left(\beta_3^{F} \mathbf{v}, \gamma_3^{I} \mathbf{w}\right)_{B_3} + \left(\beta_3^{F} \mathbf{w}, \gamma_3^{I} \mathbf{v}\right)_{B_3}. \end{aligned} \tag{A18}$$

Then from (A3a), (A4c) and (A8) we have

$$\begin{aligned} f^*(\mathbf{w}) &= \left[\mathbf{p} - \dot{\mathbf{T}}^{>}, \nabla(\Pi \mathbf{w})\right]_{H \otimes H} + (\mathbf{b}, \Pi \mathbf{w})_H \\ &\quad + \left(\dot{\mathbf{s}}, \beta_2^{\alpha} \circ \Pi \mathbf{w}\right)_{B_2} + \left(\mathbf{v}_{init}, \beta_3^{F} \mathbf{w}\right)_{B_3} + \left(\rho \mathbf{a}_{init}, \gamma_3^{F} \mathbf{w}\right)_{B_3}. \end{aligned} \tag{A19}$$

Finally, we verify that the operators given by (A16) have the dense range property, that is, that $Rg(\kappa_j|_{V_j})$ is dense in X_j, $j = 1, \ldots, 5$. Let $D_k \subset B_k, k = 1, 2, 3$, denote the smooth functions (possessing continuous partial derivatives of all orders) with compact support on the interior of Γ_k (e.g. D_2 consists of the smooth functions with compact support on $(\Sigma - \partial\Sigma) \times (0, T)$). Let any set of 10 functions $\mathbf{f}_1, \mathbf{g}_1 \in D_1, \mathbf{f}_2^{+}, \mathbf{g}_2^{+}, \mathbf{f}_2^{-}, \mathbf{g}_2^{-} \in D_2, \mathbf{f}_3^{I}, \mathbf{g}_3^{I}, \mathbf{f}_3^{F}, \mathbf{g}_3^{F} \in D_3$, be specified. Set the left-hand sides of (19), (20b) and (20c) to $\mathbf{g}_1, \mathbf{g}_2^{+}$ and $\mathbf{g}_2^{-}$, respectively.

Decompose the right-hand side gradients into normal and tangential gradients, using the decomposition $\nabla = \hat{\mathbf{n}}(\hat{\mathbf{n}}\cdot\nabla) + [(\mathbf{I} - \hat{\mathbf{n}}\hat{\mathbf{n}})\cdot\nabla]\circ\gamma_1$ on Γ_1, and make the corresponding decompositions on $\Gamma_2^{\pm}$. In (19), set the first (normal derivative) term to $\mathbf{d}_1$ and the second (tangential) term to $[(\mathbf{I} - \hat{\mathbf{n}}\hat{\mathbf{n}})\cdot\nabla]\mathbf{f}_1$, with corresponding assignments $\mathbf{d}_2^{\pm}$ and $[(\mathbf{I} - \hat{\mathbf{n}}\hat{\mathbf{n}})\cdot\nabla]\mathbf{f}_2^{\pm}$ in (20b,c). The resulting equations can be solved (using eq. 15 to invert the stress-strain relationship) to determine $\mathbf{d}_1 \in B_1$ and $\mathbf{d}_2^{\pm} \in B_2$, and we can also define $\mathbf{d}_3^I \equiv \rho^{-1}\mathbf{g}_3^I \in B_3$ and $\mathbf{d}_3^F \equiv \rho^{-1}\mathbf{g}_3^F \in B_3$. Each $\mathbf{d}_k$ is a differentiable function (since we have assumed positivity and differentiability of density, and the tensor J in eq. 15 inherits the assumed differentiability of tensor $\boldsymbol{C}$), with compact support in the interior of Γ_k (inherited from D_k). It is straightforward to construct (using a partition of unity argument, with local flatting of the boundaries Γ_1 and Γ_2, applying the fact that the support of any function in D_n is disjoint from that of any function in $D_n, n \neq m$) a $\mathbf{w} \in V$ such that $\gamma_1\mathbf{w} = \mathbf{f}_1, \gamma_2\mathbf{w} = (\mathbf{f}_2^+, \mathbf{f}_2^-), \gamma_3\mathbf{w} = \left(\mathbf{f}_3^I, \mathbf{f}_3^F\right)$, and such that the corresponding normal derivatives are $\mathbf{d}_1$, $\mathbf{d}_2^{\pm}$ and $\mathbf{d}_3^I$ and $\mathbf{d}_3^F$. This $\mathbf{w}$ will then also satisfy $\beta_1\mathbf{w} = \mathbf{g}_1, \beta_2\mathbf{w} = (\mathbf{g}_2^+, \mathbf{g}_2^-), \beta_3\mathbf{w} = \left(\mathbf{g}_3^I, \mathbf{g}_3^F\right)$. This conclusion can be summarized by defining the operator $\gamma : V \to (B_1)^2 \times (B_2)^4 \times (B_3)^4$ as

$$\gamma\,\mathbf{w} = \left(\gamma_1\mathbf{w}, \beta_1\mathbf{w}, \gamma_2^+\mathbf{w}, \gamma_2^-\mathbf{w}, \beta_2^+\mathbf{w}, \beta_2^-\mathbf{w}, \gamma_3^I\mathbf{w}, \gamma_3^F\mathbf{w}, \beta_3^I\mathbf{w}, \beta_3^F\mathbf{w}\right), \tag{A20}$$

and noting that $(D_1)^2 \times (D_2)^4 \times (D_3)^4 \subset Rg(\gamma)$. Because D_j is dense in B_j (a standard result from functional analysis, e.g. Renardy & Rogers 2004, p. 220), and each operator in (A16) is a linear combination of component operators from (A20), we have that the restriction of each κ_j to the null space of the other four has a range dense in B_j.

APPENDIX B: FRÉCHET DERIVATIVE OF EXCITATION FUNCTIONAL

Functional E is Fréchet differentiable at $\mathbf{v}_0 \in V$ if there exists a bounded linear functional d^* such that

$$\lim_{\|\mathbf{w}\|_V \to 0} \frac{|E(\mathbf{v}_0 + \mathbf{w}) - E(\mathbf{v}_0) - d^*(\mathbf{w})|}{\|\mathbf{w}\|_V} = 0, \tag{B1}$$

where $\|\cdot\|_V$ is the norm on V, in which case that d^* is the Fréchet derivative

$$DF(\mathbf{v}_0;\,\cdot) = d^*, \tag{B2}$$

(e.g. Luenberger 1969, p. 175). In the particular case where E is given by (43), we have

$$E(\mathbf{v}_0 + \mathbf{w}) - E(\mathbf{v}_0) = \int_0^T \mathrm{d}t \int_{\tilde{\Omega}} \mathrm{d}V\left(\rho_0/T\right)\mathbf{v}_0 \cdot \boldsymbol{W}\cdot\mathbf{w} + \int_0^T \mathrm{d}t \int_{\tilde{\Omega}} \mathrm{d}V\left(\rho_0/T\right)\mathbf{w}\cdot\boldsymbol{W}\cdot\mathbf{w}. \tag{B3}$$

Although we have not specified the norm on V, we stipulated in Section 3 that it be such that $\|\mathbf{w}\|_H \leq c\,\|\mathbf{w}\|_V$ for some positive constant c and all $\mathbf{w} \in V$, where $\|\mathbf{w}\|_H^2$ is the norm on H. Therefore, the last term on the right-hand side of (B3), because it is bounded by $c\|\mathbf{w}\|_H$, for some $c > 0$, must also be bounded by $c_1\|\mathbf{w}\|_V^2$, for some $c_1 > 0$, so the Fréchet derivative of E exists and is given by the first right-hand side term of (B3).

APPENDIX C: PATH SENSITIVITY KERNELS K_α and K_β

Setting $\delta\dot{\boldsymbol{C}} = \delta\boldsymbol{c}_u\delta(t)$ in (53) gives (54) and (55), which together are analogous to the modulus perturbation term of eq. (20) of Liu & Tromp (2006), together with their eq. (22). Then, following those authors, specialize to isotropy (noting that only the symmetric part of $\nabla\mathbf{v}_0$ contributes to the product) and separate $\nabla\boldsymbol{\psi}_d$: $\delta\boldsymbol{c}_u$ and the symmetric part of $\nabla\mathbf{v}_0$ into their respective isotropic and deviatoric parts. The results are analogous to eqs (25)–(28) of Liu & Tromp,

$$\delta\boldsymbol{c}_u :: \boldsymbol{K}_{\mathbf{c}} = \delta\ln\mu_u K_\mu + \delta\ln\kappa_u K_\kappa, \tag{C1}$$

$$K_\kappa(\mathbf{x}) = -\int_0^T \kappa_u \nabla\cdot\mathbf{v}_0(\mathbf{x}, T-\tau)\,\nabla\cdot\boldsymbol{\psi}_{\mathbf{d}}(\mathbf{x},\tau)\,\mathrm{d}\tau, \tag{C2a}$$

$$K_\mu(\mathbf{x}) = -\int_0^T 2\mu_u \mathbf{D}_{v_0}(\mathbf{x}, T-\tau) : \mathbf{D}_{\psi_d}(\mathbf{x},\tau)\,\mathrm{d}\tau, \tag{C2b}$$

where

$$\mathbf{D}_{\psi_d} = \frac{1}{2}\nabla\boldsymbol{\psi}_d + \frac{1}{2}(\nabla\boldsymbol{\psi}_d)^T - \frac{1}{3}\nabla\cdot\boldsymbol{\psi}_d, \tag{C3a}$$

$$\mathbf{D}_{v_0} = \frac{1}{2}\nabla\mathbf{v}_0 + \frac{1}{2}(\nabla\mathbf{v}_0)^T - \frac{1}{3}\nabla\cdot\mathbf{v}_0. \tag{C3b}$$

If we express μ_u and κ_u in terms of the corresponding P and S wave speeds, $\alpha = \sqrt{(\kappa_u + 4\mu_u/3)/\rho}$ and $\beta = \sqrt{\mu_u/\rho}$, we obtain $\delta\boldsymbol{c}_u :: \boldsymbol{k}_c$ in the alternative form $\delta\ln\alpha K_\alpha + \delta\ln\beta K_\beta$, with the S and P path kernels given by eqs (31) and (32) of Liu & Tromp,

$$K_\beta = 2\left(K_\kappa - \frac{4}{3}\frac{\mu_u}{\kappa_u}K_\kappa\right), \tag{C4a}$$

$$K_\alpha = 2\left(1 + \frac{4}{3}\frac{\mu_u}{\kappa_u}\right) K_\kappa. \tag{C4b}$$

SUPPORTING INFORMATION

Additional Supporting Information may be found in the online version of this article:

Movie S1. Animation of an elastodynamic simulation of ShakeOut V1.2b, showing the horizontal ground velocity in the N 130°E-direction and seismograms at a few selected sites. Note that the colour map saturates at ± 0.3 m s^{-1}. The thin black line shows the portion of the Southern San Andreas fault that ruptured in the scenario.
Movie S2. Animation of adjoint simulation for feature excitation in the Los Angeles basin, showing the horizontal ground velocity in the N 130°E-direction and the adjoint horizontal shear stress on the surface of the Southern San Andreas fault. Both colour maps saturate at their maximum value.
Supplement S1. Zipped Keyhole Markup Language, for use in Google Earth® and other similar software; we tested this file with Google Earth v. 6.2. Ground overlays of the path sensitivity kernel and shear-wave velocity maps (Figs 6a–c and 8a–c of the main article) in KMZ format. The fault segment that ruptured in these scenarios and the spatial windows used for the definition of the excitation functionals are also included in this file.

Please note: Wiley-Blackwell are not responsible for the content or functionality of any supporting materials supplied by the authors. Any queries (other than missing material) should be directed to the corresponding author for the article.